

$e^+e^- \rightarrow ZH$ at NLO EW matched to a QED parton shower

Lois Flower¹ and Marek Schönherr²

¹Department of Mathematical Sciences, University of Liverpool, Liverpool L69 3BX, UK

²Institute for Particle Physics Phenomenology, Department of Physics, Durham University, Durham, DH1 3LE, UK

Abstract: To prepare for the next generation particle collider, likely to be a high-energy precision-frontier electron-positron machine, theoretical predictions must improve in tandem. One aspect in which it is necessary to build on the progress made at LEP and at low-energy e^+e^- colliders is in the modelling of initial-state QED radiation from leptons. In this paper we combine the MC@NLO parton shower matching method with QED resummation methods such as the electron structure function to obtain an automated, process-independent NLO-matched QED parton shower. The case of an electron-positron collider provides a particular challenge to the method due to the integrable singularity present in the lepton structure function, at variance with QCD PDFs. We develop new methods to allow a standard dipole parton shower to operate in the presence of this singularity. We validate the method by examining its dependence on infrared parameters and by verifying both the NLO-correctness, and the resummation properties, of the MC@NLO prediction. Finally, we present results for the case of Higgs production in association with an on-shell Z boson at two proposed FCC-ee energies, the first such predictions at EW NLO+PS accuracy.

Contents

| | | |
|----------|--|-----------|
| 1 | Introduction | 2 |
| 2 | Methods | 3 |
| 2.1 | Construction of a QED dipole shower | 4 |
| 2.2 | The electron structure function | 8 |
| 2.3 | The MC@NLO method at NLO EW | 11 |
| 2.4 | Scale choices | 12 |
| 2.5 | α and electroweak input schemes | 13 |
| 3 | Validation: $e^+e^- \rightarrow \nu_\mu\bar{\nu}_\mu$ | 14 |
| 3.1 | Variation of infrared parameters | 15 |
| 3.1.1 | The shower infrared cutoff t_c | 15 |
| 3.1.2 | The ϵ structure function parameter | 16 |
| 3.1.3 | The δ parameter/parton shower x_{\max} | 16 |
| 3.2 | Validating the MC@NLO implementation of the shower | 19 |
| 4 | ZH production at a future e^+e^- collider | 22 |
| 4.1 | Threshold production: 240 GeV | 22 |
| 4.2 | Radiative production: 365 GeV | 24 |
| 5 | Conclusions | 26 |
| A | KP terms in the presence of lepton structure functions | 28 |
| B | Splitting functions | 30 |
| C | Usage and settings | 32 |

1 Introduction

Modern particle collider experiments, such as those at the Large Hadron Collider and electron-positron ‘ b factories’, are operating in a precision era in which the experimental error on many measurements is smaller than the theoretical error on the Standard Model prediction. In addition to this success of current experiments, there are a wealth of proposals for a future electron-positron collider, which would provide the most precise measurements yet of the Standard Model, and any physics beyond it. Among the most promising concepts is the future circular collider, FCC-ee, which is proposed to run at five different centre-of-mass energies, each with unique physics and precision goals [1]. This situation presents a challenge to the theory and phenomenology community.

The last 20 years have seen a plethora of new methods for increasing theoretical precision, in many cases in a largely automated and process-independent way. The POWHEG [2] and MC@NLO [3] methods allowed the combination of NLO QCD calculations with the widely used parton shower method for numerical resummation of soft and collinear logarithms and description of multiple jet production. Other NLO+PS matching methods have been developed since, such as KRKNLO [4], UNLOPs [5], multiplicative-accumulative matching [6], and ESME [7]. Similarly, the development of the multijet merging method [8, 9, 10, 11, 12], and its NLO extension [5, 13, 14, 15, 16], allowed the combination of dedicated calculations for different numbers of QCD jets, vastly improving agreement with data for multijet processes.

In addition to the improved combination of fixed-order results with resummation, there have recently been a large number of NNLO QCD predictions for many relevant processes. In particular, the ZH production process has attracted recent interest [17, 18]. By a simple power counting, it is clear that for processes involving colour-neutral particles, the NLO EW corrections are at least as important as the NNLO QCD

corrections. Not only this, but for electron-positron colliders, it is essential to model QED radiation from the initial states since it changes the centre-of-mass energy of the collision. This process is known as radiative return, and must be well-understood to make precise predictions. In particular, for the determination of the luminosity of a future lepton collider using the Bhabha scattering and diphoton measurements, a relative uncertainty of 10^{-4} (0.1 per mille) will be required [1].

The established methods for modelling QED initial-state radiation are the structure function method [19] and the Yennie-Frautschi-Suura (YFS) method [20]. The former entails exactly solving the DGLAP equations for an electron or positron in the leading-logarithmic approximation using the leading-order initial condition. The latter takes a different approach, exponentiating real and virtual soft divergences to all orders in QED and leaving the remainder as a reordered perturbative expansion. In this way, higher-order terms can be neglected whilst still including their logarithmically-enhanced contributions. The algorithmic formulation of YFS for event generation has been implemented in KKMC [21] and in SHERPA [22].

In this study, we will instead make use of the structure function, by using it (analogously to hadronic parton distribution functions) as a basis for a QED parton shower which we will match to an NLO electroweak calculation. Our approach is based on the backward-evolution paradigm [23] and is the first QED parton shower for initial-state leptons to do so. We note that an NLO-matched QED parton shower which uses forward evolution to numerically solve the DGLAP equations has existed for some time in the event generator BABAYAGA [24], which is widely used for predictions at b factories and at other low-energy e^+e^- colliders. The NLO-matched parton shower within BABAYAGA was recently extended to some $2 \rightarrow 3$ Born processes, in particular $e^+e^- \rightarrow \mu^+\mu^-\gamma$ and $e^+e^- \rightarrow \pi^+\pi^-\gamma$ [25], both of which are essential input for the interpretation of data from low-energy electron-positron colliders and the subsequent extraction of physical parameters. Comparisons between the predictions of BABAYAGA and SHERPA for the initial-state matched QED shower, and the YFS prediction, are left to a future publication. In ref. [26], a comparison of the YFS method with the matched QED shower for final-state leptons was made. A comparison of BABAYAGA's matched parton shower with other Monte Carlo codes for low-energy lepton and pion production was made in ref. [27].

This paper proceeds as follows: in section 2 we introduce the parton shower, the MC@NLO method, and the particular considerations relevant for an initial-state shower for e^+e^- ; we then present a validation of the methods in section 3 followed by phenomenological results for ZH production at a future lepton collider in section 4. Finally, we offer some concluding remarks in section 5.

2 Methods

In this section we discuss the construction of a QED dipole shower that is suitable to describe soft-collinear radiation at e^+e^- colliders, using the backward evolution formulation for initial state partons that is the *de facto* standard at hadron colliders. We focus in particular on those initial state radiation aspects that cannot be directly ported from QED parton showers for hadron colliders to lepton initial states due to the significantly different behaviour of the lepton structure function as opposed to the hadron (e.g. proton, neutron, or pion) one. Final state radiation, on the other hand, follows the familiar pattern.

We construct our QED dipole shower in full analogy to existing QCD parton showers. In particular, we choose our splitting functions to be the Catani-Seymour dipoles [28, 29] in their QED translation of [30]. Thus, following established notation, we will denote a final-state dipole splitting process as $\tilde{ij}(\tilde{k}) \rightarrow ij(k)$, i.e. the splitting of parton¹ \tilde{ij} into partons i and j in the presence of spectator parton \tilde{k} , labelled k after absorbing the transverse recoil of the splitting process. The corresponding splitting function is $S_{\tilde{ij}(\tilde{k}) \rightarrow ij(k)}$. Momenta, masses and other quantities in splitting processes are labelled with the splitting index. Likewise, initial state splittings are denoted as $a(b) \rightarrow \tilde{a}j^*(\tilde{b})$, with splitting function $S_{a(b) \rightarrow \tilde{a}j^*(\tilde{b})}$, where the parton marked with an asterisk will enter the reduced hard scattering process. Note that due to the backward-evolution algorithm, partons ‘before’ and ‘after’ the splitting are reversed in the case of initial-state splittings. Depending on whether the emitter, and the spectator, are in the initial or final state, the dipoles have different forms. All four different types of dipole are shown in Fig. 1.

¹In this paper we denote as *parton* any short-distance particle of the model under consideration. In particular, in the case of leptons and photons this helps to draw a clear distinction between, e.g., long-range beam electrons and short-distance partonic electrons that are extracted from them through the electron structure function, or, similarly, long-range detectable on-shell photons and short-distance partonic photons that may still split. They are connected through the use of structure (initial state) or fragmentation (final state) functions [31].

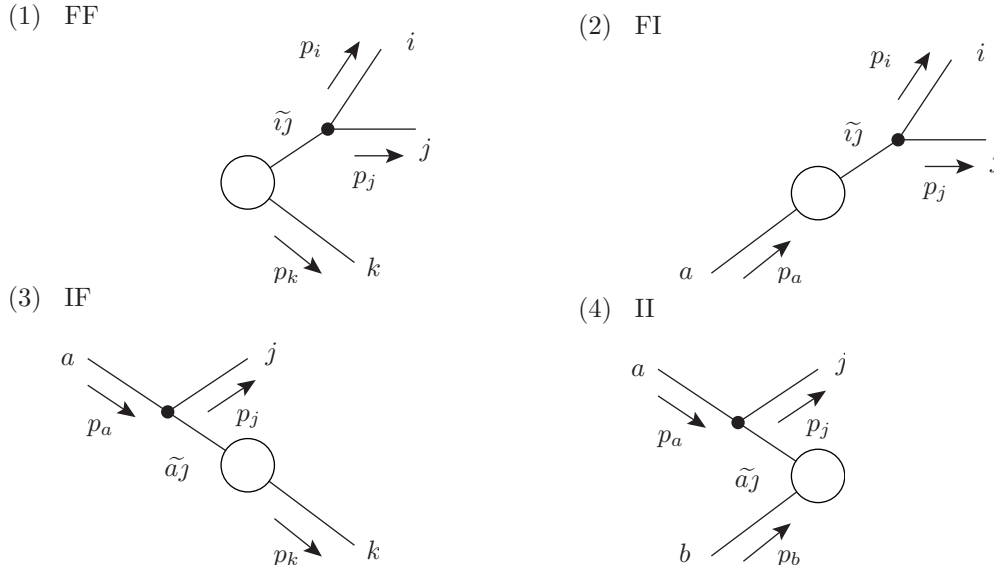


Figure 1: Dipole configurations of the Catani-Seymour splitting functions.

2.1 Construction of a QED dipole shower

In implementing a QED parton shower based on Catani-Seymour dipoles, we follow the construction paradigm of the existing CSSHOWER, within SHERPA, for QCD evolution [32], where first steps towards the incorporation of some QED evolution effects relevant for hadron colliders were taken in [33]. At variance with a QCD dipole shower, however, where the utilisation of the $N_c \rightarrow \infty$ limit results in positive (semi-)definite splitting functions, no such simplification exists for QED dipoles. The standard veto algorithm, which forms the basis of all modern parton and dipole showers [34, 35, 36], thus cannot be straightforwardly applied and its weighted generalisation [33, 37, 38, 39] has to be used.

The standard veto algorithm. The veto algorithm is used in parton showers to efficiently integrate, or sample from, an exponentially decaying function. To simplify the notation, we assume the presence of only one splitting function f without flavour changes, integrated over all degrees of freedom other than the evolution variable t . The extension to multiple functions, including flavour-changing splittings, is straightforward. This splitting function determines the probability $\mathcal{P}(t, t_0)$ of a splitting to occur at a scale t if the evolution begins at a starting scale t_0 ,

$$\mathcal{P}(t, t_0) = f(t) \exp \left[- \int_t^{t_0} d\tilde{t} f(\tilde{t}) \right] = \frac{d\Delta(t, t_0)}{dt} \quad \text{with} \quad \Delta(t_0, t) = \exp \left[- \int_t^{t_0} d\tilde{t} f(\tilde{t}) \right] \quad (2.1)$$

where $\Delta(t, t_0)$ is the Sudakov factor implementing that no branching occurred during the evolution from t_0 to t . Selecting from this distribution is straight forward, provided the integral of the splitting function, F , and its inverse, F^{-1} , are known. The evolution scales t are then determined according to

$$t = F^{-1}(F(t_0) + \log \#), \quad (2.2)$$

where $\#$ is a uniformly distributed random number on $[0, 1]$.

Unfortunately, in real applications, neither F nor F^{-1} are known. In its place, an overestimate $g(t) \geq f(t)$ is defined, where the integral G of the overestimate and its inverse G^{-1} are known. We can now propose the new splitting scale t according to Eq. (2.2) using G and G^{-1} instead. This new scale, and the associated splitting, is accepted with probability $w_{\text{acc}}(t) = f(t)/g(t)$. If the proposed splitting at scale t is instead rejected, the evolution continues from this scale, and a new proposal \tilde{t} is generated.

That this algorithm gives the correct probability of a single splitting, $\mathcal{P}(t, t_0)$, can be explicitly verified. We compute the probability of a splitting being accepted with N intermediate rejections,

$$\mathcal{P}_N(t, t_0) = \frac{f(t)}{g(t)} g(t) \exp \left[- \int_t^{t_0} d\tilde{t} g(\tilde{t}) \right] \prod_{i=1}^N \left\{ \int_{t_{i+1}}^{t_i} dt_i \left(1 - \frac{f(t_i)}{g(t_i)} \right) g(t_i) \exp \left[- \int_{t_i}^{t_{i-1}} d\tilde{t} g(\tilde{t}) \right] \right\}, \quad (2.3)$$

and then sum over all possible intermediate rejections. Identifying $t = t_{N+1}$, and using symmetry under $t_i \leftrightarrow t_j$ in the product of integrals in the second term, this gives

$$\sum_{N=0}^{\infty} \mathcal{P}_N(t, t_0) = f(t) \exp \left[- \int_t^{t_0} d\tilde{t} g(\tilde{t}) \right] \sum_{N=0}^{\infty} \frac{1}{N!} \left(\int_t^{t_0} d\tilde{t} [g(\tilde{t}) - f(\tilde{t})] \right)^N = \mathcal{P}(t, t_0). \quad (2.4)$$

This is exactly the probability distribution we sought to generate. The evolution of this newly generated state continues from the scale t as its starting scale. Once the infrared cutoff, t_c is reached, the evolution stops. This scale regularises the infrared divergences of the splitting functions by delineating the regime of resolved emissions, with $t > t_c$, from the unresolved emissions with $t < t_c$. Through the unitarity of the above veto algorithm, expressed as probability conservation, the Sudakov factor $\Delta(t_c, t_0)$ contains the soft-collinear approximation to the sum of virtual and unresolved emission corrections.

However, in showing that the veto algorithm reproduces the desired splitting probability, we have made two crucial assumptions. First, in order to generate the proposed splitting scale t , we need to require $g(t) \geq 0$ on $[t, t_0]$, such that the overestimated splitting probability is a probability density. Second, in order for the acceptance/rejection step to work, we not only need $g(t) \geq f(t)$, but also $1 \geq w_{\text{acc}}(t) = f(t)/g(t) \geq 0$. Hence, this algorithm in its minimal form is unsuitable to generate negative splitting functions in particular.

The weighted veto algorithm. We now seek to lift these restrictions on the veto algorithm and extend it to splitting functions that are negative valued, $f(t) < 0$ [37, 38, 39]. In the context of QED radiation in a dipole picture, this situation can occur when there are more than two charged particles in the process. This can be seen explicitly from the definition of the charge correlator, Eq. (B.1).

The weighted veto algorithm now introduces a second overestimate $h(t)$, with known integral H and inverse H^{-1} , that is used to generate a proposed splitting scale t through Eq. (2.2) using H and H^{-1} . However, this scale is accepted with $w_{\text{acc}}(t) = f(t)/g(t)$ as before. With this modification, the probability of accepting a splitting scale t after N rejections becomes

$$\mathcal{P}_N(t, t_0) = \frac{f(t)}{g(t)} h(t) \exp \left[- \int_t^{t_N} d\tilde{t} h(\tilde{t}) \right] \prod_{i=1}^N \left\{ \int_{t_{i+1}}^{t_{i-1}} dt_i \left(1 - \frac{f(t_i)}{g(t_i)} \right) h(t_i) \exp \left[- \int_{t_i}^{t_{i-1}} d\tilde{t} h(\tilde{t}) \right] \right\}, \quad (2.5)$$

again with $t = t_{N+1}$. We see that we recover the correct expression for the splitting probability $\mathcal{P}(t, t_0)$ when for every accepted splitting scale t , we apply the weight

$$w_N(t, t_N, \dots, t_1, t_0) = \frac{g(t)}{h(t)} \prod_{i=1}^N \frac{g(t_i) h(t_i) - f(t_i)}{h(t_i) g(t_i) - f(t_i)}, \quad (2.6)$$

where the product is over every rejected scale t_i , up to the total number N of rejected splittings. This gives

$$w_N \mathcal{P}_N(t, t_0) = f(t) \exp \left[- \int_t^{t_N} d\tilde{t} h(\tilde{t}) \right] \prod_{i=1}^N \left\{ \int_{t_{i+1}}^{t_{i-1}} dt_i \left(1 - \frac{f(t_i)}{h(t_i)} \right) h(t_i) \exp \left[- \int_{t_i}^{t_{i-1}} d\tilde{t} h(\tilde{t}) \right] \right\}, \quad (2.7)$$

and, after summing over N from zero to infinity, the correct expression for $\mathcal{P}(t, t_0)$.

Again, we have made implicit assumptions. We require $h(t) \geq 0$ on $[t, t_0]$, such that the overestimated splitting function is still a probability density. In addition, $0 \leq f(t)/g(t) \leq 1$ must hold so that the accept/reject step is probabilistically meaningful. In practice, in cases where the charge correlator is the only source for a negatively-valued splitting function, we choose $h(t)$ as the traditional overestimate for $|f(t)|$ and $g(t) = -h(t)$. With this choice the acceptance weight is always -1 and each rejection weight is strictly positive. However, with the weighted veto algorithm we no longer have the requirement that $g(t)$ must be analytically integrable — it is not used until the accept/reject step — so it can be more efficient to choose $g(t) = cf(t)$. With this option, to avoid large or diverging rejection weights where $f(t)$ and $g(t)$ coincide, we choose $c \approx 2$. We use this option in the MC@NLO matched emission.

Evolution variable. The choice of the evolution variable t is one of the defining properties of any parton shower algorithm as it defines the quantity that is resummed in its Sudakov factor. Here we follow similar

choice made in the QCD showers, which generally fall under the category of transverse momentum ordered showers [32], but to which various modifications have been made [40, 41, 42]. For initial-state splittings $a(b) \rightarrow \tilde{a}j^*j(\tilde{b})$, we distinguish two cases, choosing the modified transverse momentum \bar{k}_T^2 if a soft-photon singularity is present in the splitting function, and the reduced virtuality \bar{q}^2 otherwise, defined as

$$\begin{aligned} t_{f \rightarrow f^* \gamma} &= \bar{k}_T^2 = (Q^2 - m_f^2 - m_b^2) \frac{y}{z} (1 - z) \\ t_{f \rightarrow \gamma^* f} &= \bar{q}^2 = (Q^2 - m_f^2 - m_b^2) \frac{y}{z} \\ t_{\gamma \rightarrow f^* \bar{f}} &= \bar{q}^2 = (Q^2 - 2m_f^2 - m_b^2) \frac{y}{z} + 2m_f^2. \end{aligned} \quad (2.8)$$

Likewise, for final state splittings $\tilde{ij}(\tilde{k}) \rightarrow ij(k)$ we distinguish two cases,

$$\begin{aligned} t_{f \rightarrow f \gamma} &= \bar{k}_T^2 = (Q^2 - m_f^2 - m_k^2) y (1 - z) \\ t_{\gamma \rightarrow f \bar{f}} &= \bar{q}^2 = (Q^2 - 2m_f^2 - m_k^2) y + 2m_f^2, \end{aligned} \quad (2.9)$$

In the above, Q^2 is the dipole invariant mass, z is the light-cone momentum fraction retained by the emitting parton in the splitting process, and y is the remaining dipole variable. Their precise definitions depend on the dipole type and are given in App. B.

The use of the reduced virtuality in photon splittings further resums higher-order logarithms originating in the QED β -function [43]. Similar arguments apply to the choice of the argument of the coupling α . Photon emissions couple with $\alpha(0)$, since the photon wavefunction renormalisation cancels the light-fermion logarithms which appear. Photon splittings, on the other hand, couple with $\alpha(t')$ for a splitting at scale t' . Where a photon was produced by a parton shower emission at scale t and later splits at scale t' , its coupling should be retrospectively rescaled by $\alpha(t)/\alpha(0)$.

These choices, together with the splitting functions detailed below, ensure the correct coherence in the soft-photon limit, and angular ordering of successive emissions where appropriate. We note at this point that, since we restrict ourselves to the use of an electron structure function only (see Sec. 2.2), the initial state photon density is strictly zero. In consequence, only the splittings that use the first definition of the evolution variable in Eq. (2.8), $t_{f \rightarrow f^* \gamma}$ are present in the results presented in this paper.

Infrared cutoff. In QCD showers, the infrared cutoff t_c of the perturbative evolution is dictated by the transition from perturbative QCD, where quarks and gluons are the relevant degrees of freedom, to non-perturbative QCD and the colour-confined regime, where hadrons are the physical objects. Therefore, t_c is usually placed at scales around 1 GeV and is subject to the tuning of the non-perturbative models [44, 45, 46]. Conversely, QED is infrared free and perturbative throughout—leptons and photons remain the relevant physics objects at long distance. Hence, the IR cutoff needs only to play its role as IR regulator and must be set low enough to not interfere with physical processes of interest, including soft-photon emission and photons splitting into electron-positron pairs. We, thus, set the default IR cutoff for splittings involving only leptons and photons to a value near the electron mass. Nonetheless, the IR cutoff for photon emissions off quarks and photons splitting into quark-antiquark pairs remains at the order of 1 GeV, in order to not interfere with their hadronisation process. We will investigate the possible choices of the IR cutoff in Sec. 3.

Splitting functions and kinematics. Finally, we introduce the parton shower splitting functions that recreate the soft and collinear limits of matrix elements with one additional emission. We start by considering the soft-collinear limit of the $(n+1)$ -particle partonic cross section in terms of the n -particle partonic cross section,

$$d\hat{\sigma}_{n+1} = d\hat{\sigma}_n \otimes \sum_{\{\tilde{a}, \tilde{b}\}} \sum_f dt dz \frac{d\phi}{2\pi} \mathbf{S}_{a(b) \rightarrow \tilde{a}j^*f(\tilde{b})}(t, z, \phi). \quad (2.10)$$

Therein, $\mathbf{S}_{a(b) \rightarrow \tilde{a}j^*f(\tilde{b})}(t, z, \phi)$ is the matrix-valued (in spin/polarisation space) splitting operator [47, 48, 30] retaining the full dependence on the azimuthal splitting angle ϕ , and f runs over possible flavours of the emitted parton (in QED, $f = q, \ell, \gamma$). The \otimes -operator is defined in full analogy to refs. [28, 29, 48, 30]. Integrating out the dependence on the spin/polarisation of the emission, we arrive at the spin-averaged

splitting function $S_{a(b) \rightarrow \tilde{a}j f(\tilde{b})} = \langle \mathbf{S}_{a(b) \rightarrow \tilde{a}j f(\tilde{b})} \rangle$,

$$\langle d\hat{\sigma}_{n+1} \rangle = d\hat{\sigma}_n \cdot \sum_{\{\tilde{a}j, \tilde{b}\}} \sum_f dt dz S_{a(b) \rightarrow \tilde{a}j f(\tilde{b})}(t, z). \quad (2.11)$$

As $S_{a(b) \rightarrow \tilde{a}j f(\tilde{b})}$ is now a scalar quantity, the n -parton cross section now factorises completely, as a simple multiplication of two scalar numbers. The real-valued splitting function $S_{a(b) \rightarrow \tilde{a}j f(\tilde{b})}$, reduces further to the familiar unregularised Altarelli-Parisi splitting kernel \hat{P}_{af} in the collinear limit and, for $f = \gamma$ only, the (partial-fractioned) eikonal in the soft limit [28, 47, 29, 48, 30],

$$S_{a(b) \rightarrow \tilde{a}j f(\tilde{b})}(t, z) \xrightarrow{p_a \parallel p_f} \frac{8\pi \alpha}{z 2p_a p_f} \hat{P}_{\tilde{a}ja}(z) \quad \text{and} \quad S_{a(b) \rightarrow \tilde{a}j \gamma(\tilde{b})}(t, z) \xrightarrow{\frac{p_\gamma \rightarrow \lambda q}{\lambda \rightarrow 0}} \frac{8\pi \alpha}{\lambda^2 2p_a q} Q_a Q_b \frac{p_a p_b}{(p_a + p_b)q}. \quad (2.12)$$

The precise forms of all splitting functions are detailed in App. B. However, before discussing the relevant changes to the method which are necessary for initial-state leptonic evolution, we write the relevant splitting function here. For massless initial-state fermions, the splitting function we use for photon emission is²

$$S_{f(\tilde{b}) \rightarrow f^* \gamma(b)}(t, z) = \frac{8\pi \alpha}{2p_a p_j} \frac{1}{z} Q_f Q_b \left[\frac{2(z+y)}{1-z} + (1-z-y) \right], \quad (2.13)$$

where Q^2 is the dipole invariant mass, z is the light-cone momentum fraction retained by the emitting parton in the splitting process, y is the remaining dipole variable (see App. B for their definitions in terms of momenta). Finally, taking into account the initial state partonic electrons emerged from a composite beam particle, we absorb the change in structure function or PDF into our splitting function

$$\bar{S}_{a(b) \rightarrow \tilde{a}j f(\tilde{b})}(t, z) = S_{a(b) \rightarrow \tilde{a}j f(\tilde{b})}(t, z) \frac{f_a(\frac{x}{z}, t)}{f_{\tilde{a}j}(x, t)}, \quad (2.14)$$

where x is the momentum fraction of the original parton $\tilde{a}j$ and $f_{\tilde{a}j}(x, t)$ is its PDF or structure function, while $f_a(\frac{x}{z}, t)$ is the PDF or structure function of the newly produced parton a . Since the structure function approach that we adopt necessitates neglecting configurations with photon initial states, the only dipoles we need to consider specifically for initial-state radiation at lepton colliders are these photon-emission dipoles.

For the kinematics, since we want to match our shower to an exact NLO EW calculation, we choose the original dipole kinematics of [29, 32] while noting that for pure showering the alternative kinematics of [33] are also implemented.

With these splitting functions defined, we can now use the above veto algorithm to improve our leading order accurate infrared-safe observable O , described using the LO squared matrix element B on the leading order phase-space Φ_n , to include the effect of soft-collinear emissions. The LO plus parton shower prediction for O is then

$$\langle O \rangle^{\text{LOPs}} = \int d\Phi_n B(\Phi_n) \mathcal{F}_n(t_n, O), \quad (2.15)$$

where the functional

$$\mathcal{F}_n(t_n, O) = \Delta_n(t_c, t_n) O(\Phi_n) + \sum_{\{\tilde{a}j, \tilde{b}\}} \sum_f \int_{t_c}^{t_n} dt \int_{z_{\min}}^{z_{\max}} dz \bar{S}_{a(b) \rightarrow \tilde{a}j f(\tilde{b})}(t, z) \Delta_n(t, t_n) \mathcal{F}_{n+1}(t, O) \quad (2.16)$$

implements the parton shower evolution, recursively progressing from the starting scale, t_n on the n -parton configuration until the (global) IR cutoff scale t_c is reached. The boundaries of the z integral, $[z_{\min}, z_{\max}]$, are given by momentum conservation [32]. The parton shower Sudakov form factor $\Delta(t, t')$, given by

$$\Delta_n(t, t') = \exp \left[\sum_{\{\tilde{a}j, \tilde{b}\}} \sum_f \int_t^{t'} d\tilde{t} \int_{z_{\min}}^{z_{\max}} d\tilde{z} \bar{S}_{a(b) \rightarrow \tilde{a}j f(\tilde{b})}(\tilde{t}, \tilde{z}) \right], \quad (2.17)$$

resums the ensuing large logarithms.

²This splitting function is modified from the original Catani-Seymour by the replacement $z \rightarrow z + y$ [42].

Efficiency and dipole identification. In the case where many charged particles are present in the parton shower evolution, considering all dipoles as possible photon emitters prohibitively impacts the numerical efficiency of the algorithm due to the consequent abundance of negatively weighted events. In particular, a photon, or gluon, of a configuration with n positively-charged and m negatively-charged external particles, which splits into a fermion-antifermion pair will create an additional $2n + 2m + 2$ opposite-sign charged and $2n + 2m$ like-sign charged dipoles.

In practice, due to the separation in scales in our strongly-ordered parton shower, and the fact that the intermediate photon or gluon is neutral, $2n + 2m$ of these dipoles pairwise largely cancel, leaving the 2 newly created dipoles in the fermion-antifermion system effectively separated from the dipoles of the system that emitted the photon or gluon. Likewise, since these $f\bar{f}$ pairs are usually produced near-collinearly, soft photon emissions will not resolve their individual charges if emitted outside the cone spanned by the dipole; this is the QED analogue of angular ordering.

The solution we adopt in our QED parton shower is to identify as spectator only the opposite-sign charge same-flavour particle which results in the smallest dipole invariant mass³. We have verified for a range of processes that all relevant distributions are statistically in agreement between the unaltered and the efficiency-improved shower.

2.2 The electron structure function

As QED is perturbative in its scale evolution, an analytic solution to the DGLAP equations can be obtained at leading-logarithmic accuracy⁴. This is the electron structure function $f_e(x, Q^2)$, where x is the momentum fraction carried by the short-distance electron and Q^2 is the scale at which the long-distance beam electron is probed, usually the hard scale of the process. Using the LO initial condition $f_e(x, m_e^2) = \delta(1 - x)$ [?], it takes the leading-logarithmic (LL) form [19]

$$f_e(x, Q^2) = \beta \frac{\exp\left(-\gamma_e \beta + \frac{3}{4}\beta_S\right)}{\Gamma(1 + \beta)} (1 - x)^{\beta-1} + \sum_{n=1}^{\infty} \beta_H^n \mathcal{H}_n(x). \quad (2.18)$$

Herein, $\beta = \frac{\alpha}{\pi} (\ln(Q^2/m_e^2) - 1)$. The soft photon residue β_S and the hard prefactor β_H can be chosen either to equal β , or $\frac{\alpha}{\pi} \ln(Q^2/m_e^2)$, independently. In this paper we will choose $\beta_S = \beta_H = \beta$. While SHERPA includes the hard coefficients \mathcal{H}_n up to $n = 3$, only the leading $n = 1$ term is included in this study.

This structure function, like the δ -function it evolved from, contains an *integrable* singularity at $x = 1$. For event generation, or numerical integration in general, the presence of this singularity poses an irreconcilable problem: phase space points within an infinitesimal distance of $x = 1$ will be assigned an infinitely large weight, overwhelming any numerical precision on the resulting contribution. Naïvely introducing a cutoff $x_{\max} < 1$ excludes an important part of the spectrum and results in a severe underestimate of the total cross section. Thus, the standard solution to this problem is to reweight a portion of the structure function.

Starting from the $x \rightarrow 1$ limit of the structure function of Eq. (2.18),

$$f_e(x, Q^2) \xrightarrow{x \rightarrow 1} \beta(1 - x)^{\beta-1}, \quad (2.19)$$

the minimalist solution [36, 52] is to reweight the original structure function by a constant in an interval $[1 - \delta, 1 - \epsilon]$, where $\epsilon, \delta \ll 1$ and $\epsilon < \delta$,

$$W_e^\lambda(x, Q^2) = \begin{cases} f_e(x, Q^2) & 0 \leq x \leq 1 - \delta \\ \lambda f_e(x, Q^2) & 1 - \delta < x \leq 1 - \epsilon \\ 0 & \text{else} \end{cases} \quad \text{with} \quad \lambda = \frac{\delta^\beta}{\delta^\beta - \epsilon^\beta}, \quad (2.20)$$

where the constant λ is defined through demanding

$$\int_{1-\delta}^1 dx W_e^\lambda(x, Q^2) = \int_{1-\delta}^1 dx f_e(x, Q^2). \quad (2.21)$$

³This scheme is similar to the one implemented in PYTHIA, where new $f\bar{f}$ pairs are tracked manually [45].

⁴An approach to obtain NLL accurate structure functions was provided in [49], while the respective NNLO fixed-order expressions were published in [50, 51].

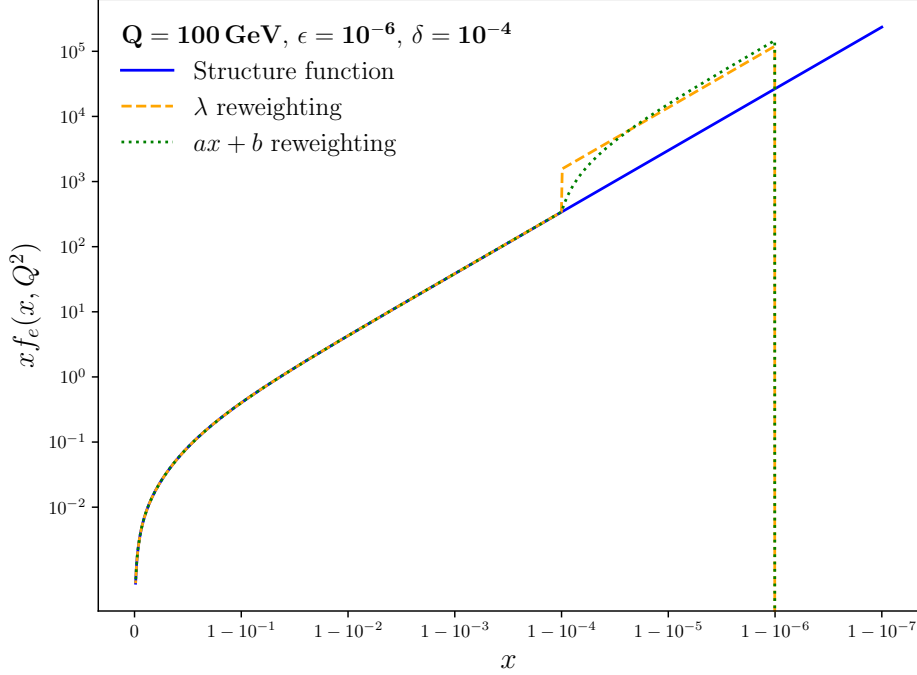


Figure 2: The electron structure function near $x = 1$, comparing different rescaling schemes. Both the x and y axes are logarithmic.

This solution preserves the total and differential cross sections as long as $\epsilon \ll \delta$ and δ is small compared to the typical resolution of the observable being calculated.⁵ However, it is important to note that the resulting rescaled structure function W_e^λ is no longer continuous nor does it satisfy the DGLAP equation. Its discontinuity at $x = 1 - \delta$ is of phenomenological importance once the momenta of the incident short-distance electrons are changed, e.g. through an initial-state parton shower. On the other hand, its violation of the DGLAP equation is expected to have negligible impact.

A solution that addresses both issues is to condense the cross section in $(\epsilon, 1]$ in a component proportional to $\delta(1 - x)$,

$$W_e^C(x, Q^2) = f_e(x, Q^2) \Theta(x \leq 1 - \epsilon) + C \delta(1 - x) \quad \text{with} \quad C = \epsilon^\beta, \quad (2.22)$$

where C is determined akin to Eq. (2.21). While continuity and adherence to the DGLAP equation for $x \in [0, 1 - \epsilon]$ is manifest in this approach and, consequently, no artifacts in initial state parton shower evolution are expected, for the case of e^+e^- collisions this results in complications in event generation as the phase space is split into four distinct and discontinuous regions,

$$(i) x_1 \leq 1 - \epsilon, x_2 \leq 1 - \epsilon; \quad (ii) x_1 \leq 1 - \epsilon, x_2 = 1; \quad (iii) x_1 = 1, x_2 \leq 1 - \epsilon; \quad (iv) x_1 = 1, x_2 = 1. \quad (2.23)$$

Thus, we pursue a different ansatz here and define

$$W_e^{ax+b}(x, Q^2) = \begin{cases} f_e(x, Q^2) & 0 \leq x \leq 1 - \delta \\ (ax + b) f_e(x, Q^2) & 1 - \delta < x \leq 1 - \epsilon \\ 0 & \text{else,} \end{cases} \quad (2.24)$$

where

$$a = \frac{(1 + \beta) \epsilon^\beta}{\delta \delta^\beta - (\delta + \beta(\delta - \epsilon)) \epsilon^\beta} \quad \text{and} \quad b = \frac{\delta \delta^\beta - (1 + \beta(1 - \epsilon)) \epsilon^\beta}{\delta \delta^\beta - (\delta + \beta(\delta - \epsilon)) \epsilon^\beta} \quad (2.25)$$

⁵The relation in Eq. (2.21) only results in the preservation of (differential) cross sections if the observable does not have significant x -dependence over the range $[1 - \delta, 1]$.

are determined by demanding equivalence, as in Eq. (2.22), and continuity at $x = 1 - \delta$, respectively. For our later application in our parton shower, this approach is sufficient to have all ingredients well-defined, when an emission crosses this threshold.

We illustrate the functional form of all three modifications of the electron structure function in Fig. 2 and demonstrate their stability in Tab. 1 and Tab. 2. Varying the technical parameters ϵ and δ across a wide range for different process at various centre-of-mass energies at electron-positron colliders, we find stable results if ϵ and δ are chosen not too large, typically $\epsilon \leq 10^{-6}$ and $\delta \leq 10^{-4}$. If δ is chosen too small, i.e. too close to ϵ , the results are statistically compatible but the uncertainty is inflated as the weighting factor, λ or a , becomes very large.

Overestimating the ratio of structure functions. As a result of the formalism of the veto algorithm in paragraph 2.1, and the definition of the initial-state splitting function in Eq. (2.14), in order to use the veto algorithm to implement our parton shower we require an analytically integrable overestimate of the splitting probability, including the ratio of the initial-state parton luminosities before and after the splitting. Since the electron structure function $f_e(x)$ is singular as $x \rightarrow 1$, this ratio can grow very large even when employing one of the methods above to regularise it, and thus overestimating it is non-trivial. In this following we present a general method relying on the asymptotic properties of the LL structure function.

Starting from the $x \rightarrow 1$ limit of the electron structure function of eq. (2.19) the luminosity ratio, including the factor $\frac{1}{z}$ present in the initial state splitting function, goes as

$$\frac{f_e\left(\frac{x}{z}, t\right)}{z f_e(x, t)} \xrightarrow{x \rightarrow 1} \frac{1}{z} \left[\frac{1-x}{1-\frac{x}{z}} \right]^{1-\beta} < \frac{1}{z} \left[\frac{1-x}{1-\frac{x}{z}} \right] < \frac{1}{z-x}, \quad (2.26)$$

where the inequalities hold since $0 < x < 1$ and $0 < z < 1$. While $\beta = \beta(t)$ itself is unknown before t is chosen, $0 < \beta < 1$ for the whole kinematic range of all colliders that can be envisioned currently. Hence we get a worst-case singularity of $(z-x)^{-1}$ in the $x \rightarrow 1$ regime. Extending it to the full x range, including hard emission corrections, we find that $k/(z-x)$ serves as an overestimate with $k \approx 10$.

The parton shower x_{\max} . With the above regularisation of the electron structure function, the effect of a parton shower emission causing a transition between $x < 1 - \delta$ and the $1 - \delta < x < 1$ region is under control. This is aided by the behaviour of the shower upon approaching this threshold. We choose to disallow any (further) evolution of an initial-state lepton which has $x \geq x_{\max} = 1 - \delta$. However, if a (potentially hard) emission would result in the production of such a lepton, it is still allowed. This choice captures the dominant contribution of the $[x_{\max}, 1]$ phase space region to the parton shower prediction and ignores only unresolvable emissions within this region.

| Process | Rescaling | Cross section (pb) | | | | |
|--|-----------|--------------------|---------------------|---------------------|---------------------|---------------------|
| | | ϵ | 10^{-9} | 10^{-8} | 10^{-7} | 10^{-6} |
| $e^+e^- \rightarrow \nu_\mu \bar{\nu}_\mu$ 91.2 GeV | λ | | 2869.0 ± 1.6 | 2869.2 ± 1.3 | 2870.5 ± 1.1 | 2869.7 ± 1.0 |
| | $ax + b$ | | 2868.3 ± 1.6 | 2870.4 ± 1.5 | 2870.0 ± 1.1 | 2869.9 ± 1.0 |
| $e^+e^- \rightarrow \nu_\mu \bar{\nu}_\mu$ 500 GeV | λ | | 0.8370 ± 0.0005 | 0.8368 ± 0.0003 | 0.8368 ± 0.0003 | 0.8371 ± 0.0003 |
| | $ax + b$ | | 0.8370 ± 0.0004 | 0.8368 ± 0.0003 | 0.8366 ± 0.0003 | 0.8373 ± 0.0003 |
| $e^+e^- \rightarrow ZH$ 365 GeV | λ | | 0.1209 ± 0.0006 | 0.1212 ± 0.0006 | 0.1220 ± 0.0006 | 0.1223 ± 0.0006 |
| | $ax + b$ | | 0.1210 ± 0.0007 | 0.1211 ± 0.0006 | 0.1218 ± 0.0007 | 0.1219 ± 0.0007 |

Table 1: Leading-order cross sections in the G_μ scheme using AMEGIC. ϵ is varied between 10^{-9} and 10^{-6} , and $\delta = 10^{-4}$ is used throughout. The errors are statistical uncertainties on the Monte Carlo integration.

| Process | Rescaling | Cross section (pb) | | | | |
|---|-----------|--------------------|---------------------|---------------------|---------------------|---------------------|
| | | δ | 10^{-7} | 10^{-6} | 10^{-5} | 10^{-4} |
| $e^+e^- \rightarrow \nu_\mu\bar{\nu}_\mu$ 91.2 GeV | λ | | 2876.0 ± 7.0 | 2870.7 ± 3.3 | 2872.0 ± 1.8 | 2872.1 ± 1.2 |
| | $ax + b$ | | 2871.1 ± 8.0 | 2873.0 ± 3.8 | 2871.6 ± 2.1 | 2871.6 ± 1.2 |
| $e^+e^- \rightarrow \nu_\mu\bar{\nu}_\mu$ 500 GeV | λ | | 0.8393 ± 0.0012 | 0.8381 ± 0.0007 | 0.8376 ± 0.0005 | 0.8375 ± 0.0003 |
| | $ax + b$ | | 0.8400 ± 0.0014 | 0.8384 ± 0.0007 | 0.8378 ± 0.0005 | 0.8376 ± 0.0004 |
| $e^+e^- \rightarrow ZH$ 365 GeV | λ | | 0.1236 ± 0.0010 | 0.1235 ± 0.0005 | 0.1230 ± 0.0003 | 0.1231 ± 0.0002 |
| | $ax + b$ | | 0.1248 ± 0.0012 | 0.1236 ± 0.0006 | 0.1232 ± 0.0003 | 0.1230 ± 0.0002 |

Table 2: Leading-order cross sections in the G_μ scheme using AMEGIC. δ is varied between 10^{-7} and 10^{-4} , and $\epsilon = 10^{-8}$ is used throughout. The errors are statistical uncertainties on the Monte Carlo integration.

2.3 The MC@NLO method at NLO EW

The MC@NLO method [3], in particular in the variant implemented in SHERPA [37, 53], allows the automated matching of an NLO QCD calculation to a parton shower in a process-independent way. With the QED parton shower of the previous section at hand, we are now in a position to extend it to match NLO EW corrections for electron-positron collider processes, although purpose-built NLOPS calculations for selected processes, $e^+e^- \rightarrow f\bar{f}(\gamma)$, $e^+e^- \rightarrow \gamma\gamma$, and more recently $e^+e^- \rightarrow \pi^+\pi^-(\gamma)$, exist in the event generator BABAYAGA [24, 54, 55, 25]. In this section, we describe the MC@NLO method for electroweak corrections as implemented in SHERPA, and highlight its differences with respect to its established NLO QCD sister.

The core idea of the MC@NLO method is to use the parton shower to subtract all divergences at NLO. To this end, in full analogy to Eq. (2.16), we introduce the modified parton shower functional

$$\bar{\mathcal{F}}_n(t_n, O) = \bar{\Delta}_n(t_c, t_n) O(\Phi_n) + \sum_{\{\bar{a}_j, \bar{b}\}} \sum_f \int_{t_c}^{t_0} dt dz \frac{d\phi}{2\pi} \bar{\mathbf{S}}_{a(b) \rightarrow \bar{a}_j f(\bar{b})}(t, z, \phi) \bar{\Delta}_n(t, t_n) \mathcal{F}_{n+1}(t, O). \quad (2.27)$$

Instead of the spin-averaged splitting functions, this modified shower uses the full spin-dependent variants $\mathbf{S}_{a(b) \rightarrow \bar{a}_j f(\bar{b})}$,⁶ augmented with the corresponding initial-state luminosity ratio as in Eq. (2.14). This form captures the full infrared divergence structure at NLO EW. Likewise, its Sudakov factor is defined as

$$\bar{\Delta}_n(t', t_c) = \exp \left[\sum_{\{\bar{a}_j, \bar{b}\}} \sum_f \int_{t_c}^{t_n} dt \int_{z_{\min}}^{z_{\max}} dz \int_0^{2\pi} \frac{d\phi}{2\pi} \bar{\mathbf{S}}_{a(b) \rightarrow \bar{a}_j f(\bar{b})}(t, z, \phi) \right]. \quad (2.28)$$

Beyond NLO, if a spin-correlated emission has occurred, the standard spin-averaged parton shower \mathcal{F} continues the evolution of the $(n+1)$ -parton state. Using the functionals defined in Eq. (2.16) and Eq. (2.27), we can thus write the expectation value for an arbitrary infrared-safe observable O as

$$\langle O \rangle^{\text{MC@NLO}} = \int d\Phi_n \bar{\mathbf{B}}(\Phi_n) \bar{\mathcal{F}}_n(t_n, O) + \int d\Phi_{n+1} \mathbf{H}(\Phi_{n+1}) \mathcal{F}_{n+1}(t_{n+1}, O), \quad (2.29)$$

where the \mathbf{H} function to be defined below contains contributions in the real-emission phase space, while the $\bar{\mathbf{B}}$ function,

$$\bar{\mathbf{B}}(\Phi_n) = \mathbf{B}(\Phi_n) + \tilde{\mathbf{V}}(\Phi_n) + \sum_{a,j,b} \int d\Phi_1^{aj,b} \mathbf{D}_{aj,b}^A(\Phi_n, \Phi_1^{aj,b}), \quad (2.30)$$

collects all contributions which occur in the Born phase space. Besides the Born matrix element \mathbf{B} itself, these are the renormalised virtual correction $\tilde{\mathbf{V}}$, defined to include the collinear counterterms, and the parton shower splitting kernels integrated over the entire soft-collinear phase space up to the n -parton shower starting

⁶As this paper is largely concerned with the intricacies of an initial state QED parton shower at lepton colliders and its matching to full NLO EW correction, we have chosen to use the initial-initial dipole notation throughout. Nonetheless, the algorithm is completely general and equally applies to all four types in depicted in Fig. 1.

scale t_n ,

$$\int d\Phi_1^{aj,b} D_{aj,b}^A(\Phi_n \cdot \Phi_1^{aj,b}) = B(\Phi_n) \otimes \int_0^{t_n} dt dz \frac{d\phi}{2\pi} \bar{\mathbf{S}}_{a(b) \rightarrow \tilde{a}j \tilde{b}}(t, z, \phi). \quad (2.31)$$

By comparison with Eq. (2.10), it is evident that the infrared poles of Eq. (2.31) are identical to those of the full real-emission matrix element and, thus, cancel those of the virtual correction by virtue of the KLN theorem, rendering the $\bar{\mathbf{B}}$ function IR finite. In general, however, the coefficients of the Laurent expansion of the integrated parton shower splitting kernels in D dimensions are unknown. Hence, we employ a second subtraction,

$$\sum_{a,j,b} \int d\Phi_1^{aj,b} D_{aj,b}^A(\Phi_n \cdot \Phi_1^{aj,b}) = \sum_{\tilde{a}j, \tilde{b}} I_{\tilde{a}j, \tilde{b}}^S(\Phi_n) + \sum_{a,j,b} \int d\Phi_1^{aj,b} \left[D_{aj,b}^A(\Phi_n \cdot \Phi_1^{aj,b}) - D_{aj,b}^S(\Phi_n \cdot \Phi_1^{aj,b}) \right], \quad (2.32)$$

using the real and integrated subtraction terms, $D_{aj,b}^S$ and $I_{\tilde{a}j, \tilde{b}}^S$, of the Catani-Seymour subtraction formalism [28, 29, 30]. This allows the simple evaluation of the left-hand side of Eq. (2.32) when the choice

$$D_{aj,b}^A = D_{aj,b}^S \Theta(\mu_Q^2 - t_{aj,b}) \quad (2.33)$$

is made for the parton shower splitting kernels [37].

Turning again to the H function in Eq. (2.29), we now specify its definition as

$$H(\Phi_{n+1}) = R(\Phi_{n+1}) - \sum_{a,j,b} D_{aj,b}^A(\Phi_n^{aj,b} \cdot \Phi_1^{aj,b}), \quad (2.34)$$

with the real-emission contribution R being subtracted by the soft-collinear approximation generated by our parton shower. $\Phi_{n+1} = \Phi_n^{aj,b} \cdot \Phi_1^{aj,b}$ is the dipole-dependent factorised phase space. With these definitions for $\bar{\mathbf{B}}$ and H as well as our modified parton shower, it is straightforward to show that the $\mathcal{O}(\alpha)$ expansion of Eq. (2.29) correctly reproduces the NLO expression for any infrared-safe observable O [37].

Further, it is important to note from Eq. (2.33) the phase space limit in D^A , namely that it is strictly zero for emissions with $t > t_n$. Hence, while soft emissions will be described through our (modified) parton shower resummation in $\bar{\mathcal{F}}_n$ acting on $\bar{\mathbf{B}}$, corrected to full $\mathcal{O}(\alpha)$ accuracy by H , hard emissions are solely described by H .

The MC@NLO algorithm. The MC@NLO method according to Eq. (2.29) is implemented using the following algorithm.

1. Generate one of two types of events: either an \mathbb{S} -event (‘soft’ or ‘standard’) using the $\bar{\mathbf{B}}$ function of Eq. (2.30), or an \mathbb{H} -event (‘hard’) using the H function of Eq. (2.34). If unweighted events are sought, their relative composition should be that of their respective cross sections.
2. If an \mathbb{S} -event was chosen, feed the resulting Born-type phase space configuration to the fully spin-correlated QED parton shower $\bar{\mathcal{F}}_n$ of Eq. (2.27), using the hard scale t_n as its starting scale. If an emission is generated, pass the event to the standard shower \mathcal{F}_{n+1} which continues the evolution from the newly-generated scale t_{n+1} .
3. If an \mathbb{H} -event was chosen, pass its real-emission-type phase-space configuration directly to the standard parton shower \mathcal{F}_{n+1} . Determine its starting scale t_{n+1} by interpreting its existing emission kinematics as a parton splitting process, using the inverse of \mathcal{F}_n as a clustering algorithm [12].

2.4 Scale choices

The choice of factorisation scale in an MC@NLO EW is relevant despite the slow running of α compared to that of α_s . As has been argued [37, 56], a lack of phase-space restrictions on the exponentiated ($\bar{\mathbf{S}}$ and $\bar{\mathbf{S}}$) part of the real emission can lead to logarithmic contributions to MC@NLO of $\alpha \log^2(q^2/s)$, where q^2 is the virtuality of the emitter parton, instead of the correct parton shower contribution of $\alpha \log^2(q^2/\mu_F^2)$. This implies that where $\mu_F^2 \ll s$, a careful choice of scale is needed. The scale chosen must be soft- and

collinear-safe, so the invariant mass of bare charged particles cannot be used to define the scale. In the case of the processes studied here, we use the invariant mass of the uncharged final state as the factorisation scale.

Similarly, the shower starting scale μ_Q^2 should be a typical scale of the hard process. The purpose of this scale is twofold: to put an upper limit on the kinematics of emissions generated using splitting functions, and to ensure that the correct Sudakov factors are applied to all emissions. For these reasons, the starting scale is treated slightly differently between \mathbb{S} - and \mathbb{H} -events, in order to reflect the different physical descriptions of radiation that these imply.

In an \mathbb{S} -event, the ordinary shower must be a continuation of the MC@NLO shower, even if the splitting functions are slightly different. This results in an identification of the factorisation scale μ_F which constrains the contributions of the soft exponentiated terms D^A to be the same as the \mathbb{S} -event MC@NLO shower starting scale μ_Q . Hence, the MC@NLO shower starts from $t_n = \mu_Q^2$ and either continues to an IR cutoff (in which case the shower cannot act and there must be no further emissions), or generates an emission at t_1 . In both cases a Sudakov factor is generated. The ordinary shower then continues from $t_{n+1} = t_1$ to the infrared cutoff, which must be the same as the MC@NLO cutoff for consistency.

For the \mathbb{H} -events, to preserve the total NLO cross section, there can be no Sudakov factor applied to the first emission as there is no splitting function term to reinstate unitarity⁷. However, to avoid double counting, this emission must be reinterpreted in the parton shower language to have scale t_{n+1} . This is achieved using the MEPS clustering algorithm [57]. Now we consider the two possible cases:

$t_{n+1} < \mu_Q^2$ The shower should start from t_{n+1} , since to allow a harder emission would amount to a rejection of the matching and resummation principles by allowing an unordered configuration.

$t_{n+1} > \mu_Q^2$ This case is not clear-cut from resummation arguments. On the one hand, t_{n+1} is now the hardest scale of the process, but on the other, we would like to avoid extending the resummation beyond its region of validity. Here we choose to start the shower from t_{n+1} , which extends both the emission probability and the Sudakov factor up to the new hardest scale.

Photons at Born level. The presence of photons in the Born matrix element complicates the implementation of the MC@NLO method slightly. Clearly, the splitting of such a photon is of the same perturbative order as the emission of a photon off any charged particle in the process; however, analyses frequently use isolated or tagged hard ‘prompt’ photons. As such, events in which a Born photon splits in an \mathbb{S} -event will be rejected by the analysis criteria unless a similar photon is emitted by the parton shower. In practice, one can label a photon from the matrix element as tagged, and ensure that it becomes a long-distance photon (and couples with $\alpha(0)$). However, if the Born matrix element contains two (or more) photons, only one of which is tagged while the other may split, further consideration is needed. If photon splittings do occur, care must be taken to match their spectator schemes between the \mathbb{S} - and \mathbb{H} -events.

2.5 α and electroweak input schemes

Before presenting results from the QED parton shower and MC@NLO, we briefly discuss EW input schemes and the treatment of α . For the evaluation of MEs in hard processes, it is most appropriate to use a value of α which resums higher-order corrections. Using $\alpha(0)$ for processes at scales of the EW gauge bosons or higher leads to logarithms of the type $\log(m_f^2/m_{Z/W}^2)$, which are large for light flavours f . To include these photonic vacuum polarisation corrections to the coupling, a short-distance renormalisation scheme must be used, commonly either of the $\alpha(m_Z)$ or G_μ schemes. In particular, the G_μ scheme absorbs higher-order corrections to the renormalisation of the weak mixing angle, and thus is often the scheme of choice when a fermion interacts with a weak boson at Born level.

Since the difference between the values of α in different schemes is formally subleading, we have the freedom to define a different scheme for radiative corrections [58]. In the case of NLO calculations, of course, this must be consistent in all parts of the NLO calculation to ensure cancellation of singularities. A similar procedure was followed, for example, in refs. [59, 60, 61], to consistently use the correct α in different parts of an NLO calculation. For the case of the shower, which is unitary, we are free to use a running α in the shower, analogously to QCD. For photon emissions, since most will become long-distance photons (i.e. they

⁷In NLO merging, where the total cross section will in any case not be the NLO cross section, applying the Sudakov here is perfectly acceptable.

will not split again), their QED coupling should be evaluated in the Thomson limit, so we choose $\alpha(0)$, capturing the photon-to-photon fragmentation function to $\mathcal{O}(\alpha)$. This is because the photonic wavefunction renormalisation already exactly cancels the light-fermion logarithms in the renormalisation of the coupling constant. For photon splittings into fermions, we choose the coupling evolved to the splitting scale, $\alpha(t)$, where here t is the reduced virtuality. Further, if the splitting photon was produced with its coupling set to $\alpha(0)$, we additionally include a correction to its coupling factor of $\alpha(t_{\text{prod}})/\alpha(0)$ in its splitting function, where t_{prod} is the k_T -like scale of its radiation off a fermion. Additionally, in the electron structure function, we use $\alpha(0)$. This is consistent with physical expectations and with existing conventions.

3 Validation: $e^+e^- \rightarrow \nu_\mu \bar{\nu}_\mu$

Having outlined the necessary modifications to the MC@NLO method for use with a QED parton shower, it now remains to test the implementation and stability of the method. We will examine the dependence of our predictions on the parameters ϵ , $\delta = 1 - x_{\text{max}}$, and the infrared cutoff t_c . In addition to demonstrating the numerical stability of the method, this will inform the choice of values for these parameters to produce predictions for $e^+e^- \rightarrow ZH$ in Sec. 4. After validating the QED parton shower this way, we will test that the MC@NLO fully spin-correlated emission reproduces its results upon neglecting the hard-emission corrections which are needed to make the MC@NLO prediction correct to NLO. Finally, in the next section we will compare the LO+PS and MC@NLO predictions to the fixed-order LO and NLO for ZH production.

In the present section, we will set up simple test scenarios to examine a range of observables to validate the QED parton shower and fully spin-correlated MC@NLO. Throughout, we use the matrix element generators AMEGIC [62], COMIX [63] and OPENLOOPS [64, 65, 66, 67] for the tree-level matrix elements, renormalised one-loop amplitudes, and infrared subtraction. We use the LL electron structure function [19], see Sec. 2.2, with the electron mass parameter $m_e = 511$ keV and the dynamic scale $Q^2 = s' = m_{\nu\bar{\nu}}^2$ in the hard scattering process. We work in the complex mass scheme [68],

$$\mu_i^2 = m_i^2 - im_i\Gamma_i \quad \text{with} \quad i \in \{W, Z, H, t\}, \quad (3.1)$$

with the following masses and widths

$$\begin{aligned} m_W &= 80.370 \text{ GeV} & \Gamma_W &= 2.0897 \text{ GeV} \\ m_Z &= 91.1876 \text{ GeV} & \Gamma_Z &= 2.4952 \text{ GeV} \\ m_H &= 125.09 \text{ GeV} & \Gamma_H &= 0.0041 \text{ GeV} \\ m_t &= 172.5 \text{ GeV} & \Gamma_t &= 1.32 \text{ GeV} \end{aligned} \quad (3.2)$$

All other particles are treated massless in the perturbative matrix elements. In the parton shower, external particles are shifted onto their physical mass shells and evolve according to their massive splitting functions, detailed in App. B.

As described in Sec. 2.5, we use the G_μ scheme with $(G_\mu, \mu_W^2, \mu_Z^2)$ as our input parameter set to define and renormalise our EW parameters. The Fermi constant itself takes the value

$$G_\mu = 1.16639 \times 10^{-5} \text{ GeV}^{-2}. \quad (3.3)$$

Consequently, it defines the lowest-order couplings. To match the NLO corrections to the parton shower, however, we use the $\alpha(0)$ scheme with $(\alpha(0), \mu_W^2, \mu_Z^2)$ for the additional coupling entering at NLO and in the photon emissions in the parton shower. Their values are given by

$$\alpha_{G_\mu} = \left| \frac{\sqrt{2} s_w^2 \mu_W^2 G_\mu}{\pi} \right| \quad \text{and} \quad \alpha(0) = 1/137.03599976, \quad (3.4)$$

with the weak mixing angle

$$s_w^2 = 1 - c_w^2 = 1 - \frac{\mu_W^2}{\mu_Z^2}. \quad (3.5)$$

For simplicity and to see more clearly the effects of varying the shower parameters, we consider only photon emissions here (no photon splittings). However, these are fully implemented in the parton shower, and the

relevant switches are detailed in App. C. The effect of producing further charged-particle pairs can be very relevant depending on the observable [69], but here we focus on the radiative impacts on the initial-state particles, which translate to recoil of the entire final state; where the initial-state particles are leptons, these impacts are dominated by their photon emissions.

In order to validate the implementation of the QED parton shower for initial-state leptons, we study muon neutrino production at an electron-positron collider for two different centre-of-mass energies: $\sqrt{s} = 91.2$ GeV and $\sqrt{s} = 500$ GeV. While the former is dominated by soft radiation, the latter affords plenty of phase space and matrix element support to collinear emissions. The combination of both setups will allow us to examine the shower’s description of radiation in both limits. The choice of muon neutrinos as the final state ensures that only the s -channel Z exchange diagram contributes, which results in a clean resonance structure of the cross section and a straightforward identification of the relevant scales, see Sec. 2.4.

In addition to examining specific radiation-induced observables, we will study two which appear at LO: the neutrino-pair invariant mass $m_{\nu\bar{\nu}}$, and the (matter) neutrino transverse momentum k_{T}^{ν} . The former is completely unchanged by initial-state showering due to the specific kinematic construction of the Catani-Seymour shower, so provides a useful cross-check of the implementation and allows comparison of the LO and NLO distributions without shower effects. The latter will provide an analogue to identified-final-state transverse momenta, such as the Z transverse momentum which we will study in Sec. 4, and is, in general, modified from its fixed-order distribution by the action of a parton shower.

The radiative observables that will be presented here include the hardest photon transverse momentum $k_{\text{T}}^{\gamma} = \max(k_{\text{T}}^{\gamma i})$, the second-hardest photon transverse momentum $k_{\text{T}}^{\gamma 2}$, and the photon multiplicity N_{γ} with transverse momentum above a cut $k_{\text{T}}^{\gamma i} > k_{\text{T}}^{\text{min}}$. For this process, we choose $k_{\text{T}}^{\text{min}} = 0.5$ GeV. In addition, we examine the 0-to-1 QED jet rate d_{01} , as defined using the k_{T} clustering algorithm. In this algorithm, the distance parameter is given by

$$d_{ij} = \min(k_{\text{T}i}^2, k_{\text{T}j}^2) \frac{\Delta R_{ij}^2}{R^2}, \quad (3.6)$$

where ΔR_{ij} is the distance in pseudorapidity and azimuthal angle, $\Delta R_{ij}^2 = \Delta\eta_{ij}^2 + \Delta\phi_{ij}^2$. We use a radius parameter $R = 1$. In this process, the particles which we consider as input to the algorithm are electrons and photons. The differential jet rate $d_{n,n+1}$ measures at what scale the $(n+1)^{\text{th}}$ jet is formed, and is thus ideally suited to assess the internal dynamics of our initial state evolution. Where only photon emissions are modelled, this is equivalent to a photon- k_{T} -type observable (up to differences in the shower evolution variable), but where photon splittings are considered, the two will differ. Using a jet algorithm to define a final state means that we are inclusive with respect to flavour, analogously to QCD parton showers.

There remain some choices to be made in the shower algorithm and in the analysis, which will be informed by the results of this test process. In particular, we study the various infrared cutoff parameters, then validate the first emission in MC@NLO as a special case of the parton shower.

3.1 Variation of infrared parameters

First, we investigate the effects of the shower infrared cutoff, t_c , on the observables described above, then we study the two structure function parameters ϵ and δ defined in Sec. 2.2. To do so, we restrict ourselves to the shower acting on LO events. The NLO calculation, being afflicted with an additional integration over the same integrable divergence in the electron structure function, necessitates the introduction of another technical parameter, ε , which is detailed in App. A. We have checked that the dependence of the cross section on its value is far smaller than that for the LO parameters investigated here.

We have seen, in Tab. 1 and 2, that the variation of ϵ and δ within reasonable limits does not alter the total LO cross section. Additionally, by construction, the variation of t_c does not affect the total cross section, nor any Born-level observable with a resolution larger than t_c . However, the impact of the choice of these three variables on differential observables must be evaluated, as well as their effect on the efficiency of event generation.

3.1.1 The shower infrared cutoff t_c

In Fig. 3, we see that varying the shower infrared cutoff, t_c results in very little change to inclusive Born-level observables such as the neutrino transverse momentum, but a sharp cutoff is visible in radiative observables.

This is as expected, since the strict ordering and unitary construction of the photon-emission-only shower ensure that an emission at a given t does not affect emissions which are harder in t . The distributions in the 0-to-1 jet rate and second photon transverse momentum do not drop to zero below the cutoff, however, since neither variable corresponds exactly to the parton shower ordering variable. It is important to note that although the differential cross sections below the cutoff are not small (indeed, the underflow bin contributes most of the cross section), the kinematic impact on the rest of the event is very small for these soft photons, as illustrated by the stability of the neutrino transverse momentum. Thus, the choice of whether to produce them with the parton shower is dependent on the desired observable resolution, informed by experimental constraints such as detector limits.

The agreement in the radiative observables above the respective infrared cutoff is better than 1% for both collider energies, while the agreement in the neutrino transverse momentum is on the 0.1% level across the majority of phase space. For the remainder of this section, we will use $t_c = 10^{-6} \text{ GeV}^2$, to avoid contaminating the soft end of the spectrum when varying the other parameters. However, because of the straightforward dependence of the radiative observables on t_c , it can be varied anywhere below the sensitivity of the observable in question without introducing further uncertainties.

3.1.2 The ϵ structure function parameter

The top row of Fig. 4 shows that varying the structure function parameter ϵ does not affect Born-level observables such as the neutrino-pair invariant mass at the sub-percent level. The invariant mass is a useful observable to compare, unlike for the variation of t_c , because its dependence on ϵ enters both before the parton shower evolution and during it, due to the ratio of structure functions which appears. The parton shower evolution will never move the event in phase space up to the boundary $x = 1 - \epsilon$, but the value of ϵ affects the rescaling near the boundary, which can change the parton shower splitting probabilities.

Meanwhile, in the middle row we verify that varying ϵ between 10^{-9} and 10^{-7} does not affect the radiative distribution in the 0-to-1 jet rate, for both collider energies. In fact, we observe agreement at the sub-percent level, showing the self-consistency of our linear rescaling method. However, we see a systematic 0.5% underestimate of the jet rate for the largest ϵ value for $\sqrt{s} = 91.2 \text{ GeV}$, and a much more severe disagreement for $\epsilon = 10^{-5}$ and 10^{-6} at 500 GeV.

Similarly, in the bottom row, we show the transverse momentum of the second-hardest identified photon. It is clear that this observable is more sensitive to the structure function parameters, showing variation of a few percent for many values of ϵ . Although larger, the deviations in k_T^2 are consistent with those in d_{01} , and show that this method of rescaling the structure function is only fully stable, for $\epsilon = 10^{-8}$ compared to 10^{-9} , for photon emissions at a scale harder than 10^{-2} GeV for a collider at the 10^2 GeV scale. Photons at this scale will have almost no kinematic impact and the photon itself is very unlikely to be detectable. For the application of this method to collisions at much lower energies, the range of stable parameters will again have to be determined.

It is clear from Fig. 4 that at the Z mass, $\epsilon = 10^{-6}$ or smaller is sufficient to well-describe all studied observables, while at 500 GeV, the requirement is more stringent for radiative observables. For this reason, for the rest of this paper, we will use $\epsilon = 10^{-8}$.

3.1.3 The δ parameter/parton shower x_{\max}

The δ parameter here controls the lower limit of the structure function rescaling, as well as the upper limit on x in the parton shower, see Sec. 2.2. As a result, the aim of this validation is to find the largest value of δ which makes reliable predictions, since this will allow faster shower evolution.

In Fig. 5, we vary δ between 10^{-7} and 10^{-3} in isolation, keeping ϵ fixed at 10^{-8} as the outcome of the previous validation exercise. Since ϵ and δ enter the structure function rescaling approximately through their ratio, this should be thought of as varying the ratio between the two from 10 to 10^5 . We might expect that the behaviour could be pathological at both ends of this spectrum: if the ratio is too small, the reweighting factor differs significantly from unity, and if it is too large this implies a too-small shower x_{\max} and a poor description of radiation.

On the top row of Fig. 5, we show the neutrino-pair invariant mass and verify that this observable is invariant on the percent level under changing δ . The middle row, as before, shows the 0-to-1 jet rate. For the 91.2 GeV process, choices between 10^{-7} and 10^{-4} all agree to within 1%, but $\delta = 10^{-3}$ does not adequately describe

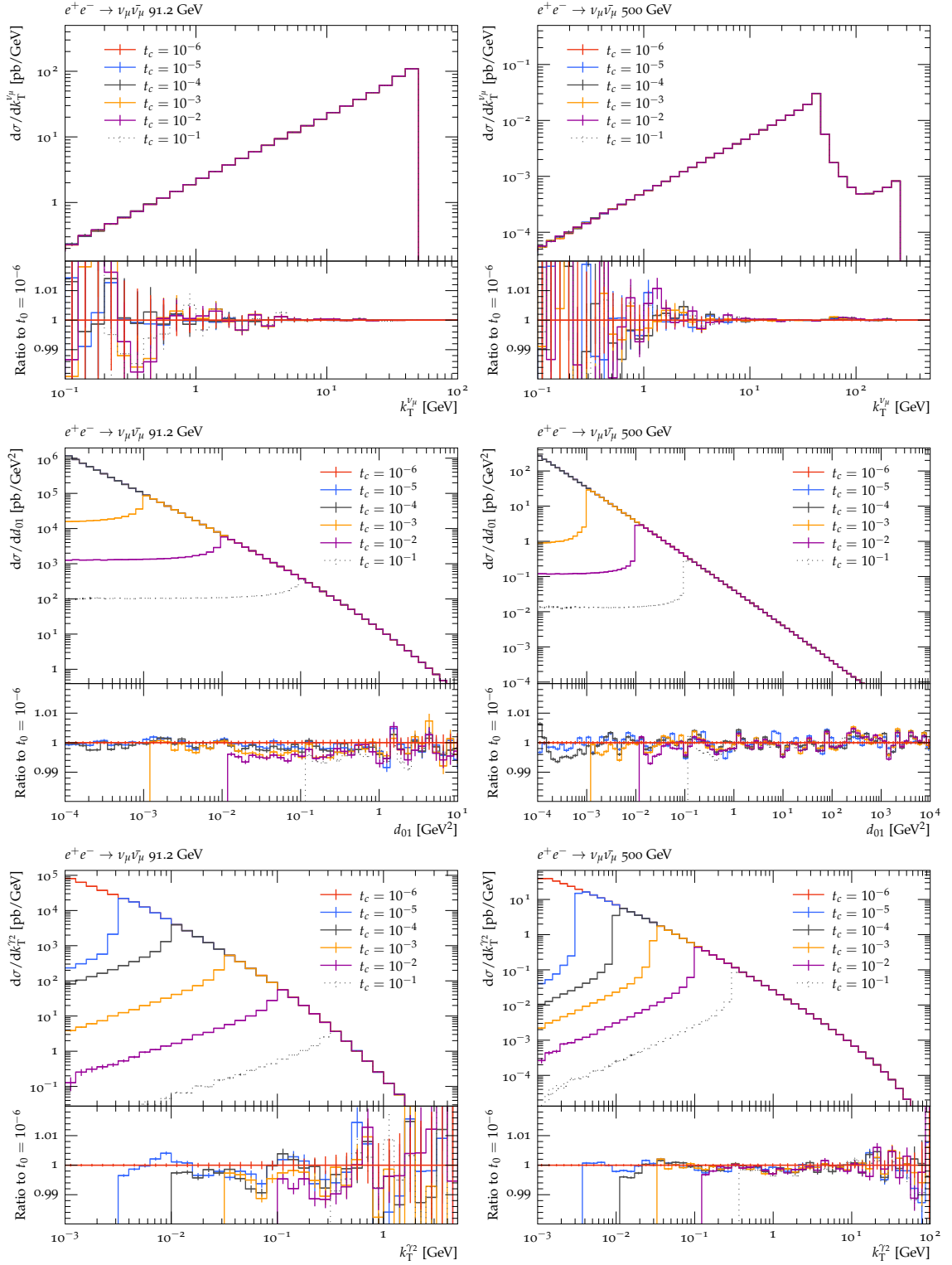


Figure 3: Plots showing the effect of varying the parton shower infrared cutoff, t_c , for the process $e^+e^- \rightarrow \nu_\mu\bar{\nu}_\mu$ at two different collider energies, 91.2 GeV (left) and 500 GeV (right). The observables shown are the neutrino transverse momentum (top row), the 0-to-1 jet rate (middle) and the second photon transverse momentum (bottom). The infrared cutoff is varied logarithmically between 10^{-6} GeV^2 and 10^{-1} GeV^2 .

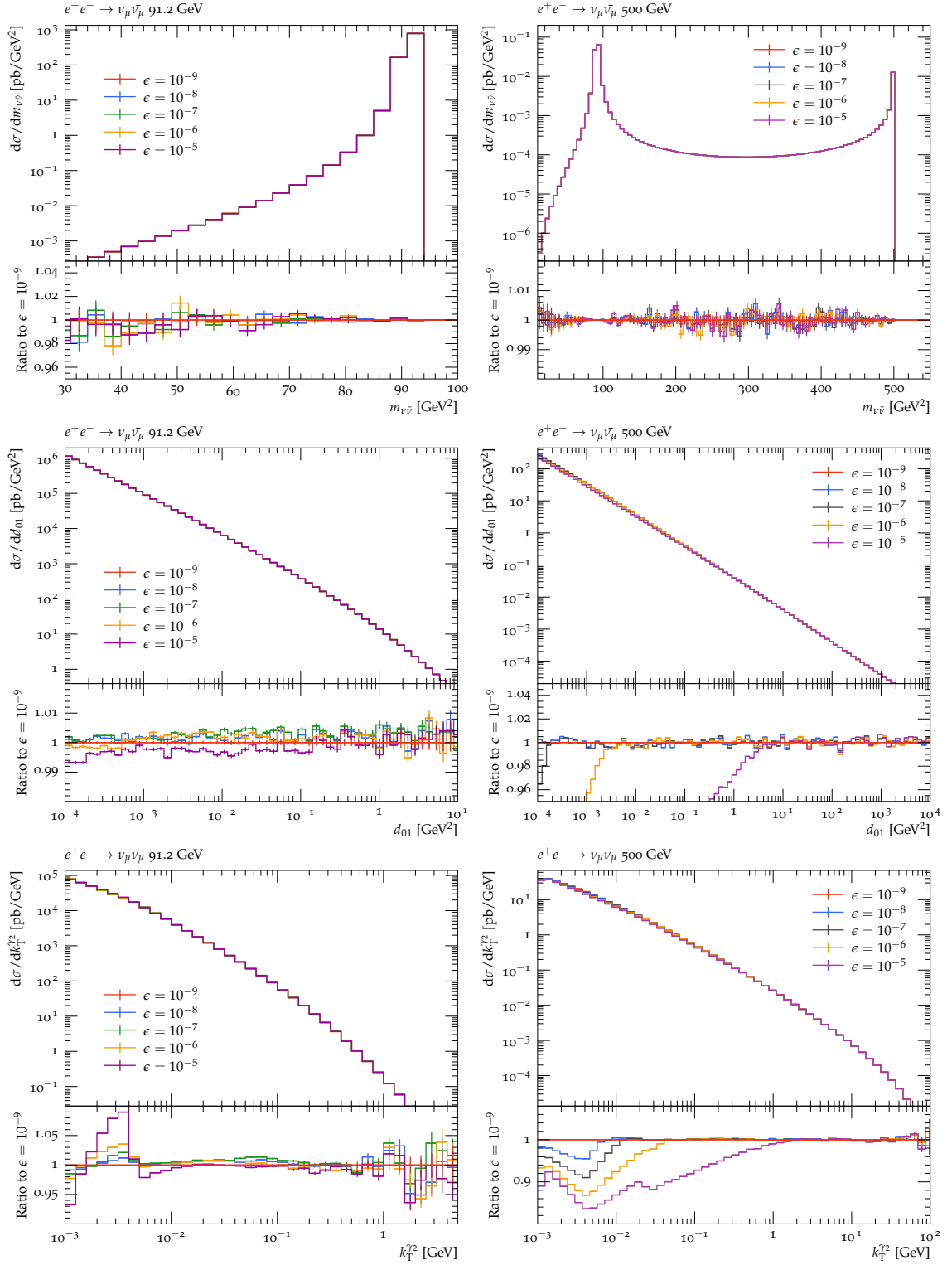


Figure 4: Plots showing the effect of varying the structure function ϵ parameter for the process $e^+e^- \rightarrow \nu_\mu \bar{\nu}_\mu$ at two different collider energies, 91.2 GeV (left) and 500 GeV (right). The observables shown are the neutrino-pair invariant mass (top row), the 0-to-1 jet rate (middle) and the second photon transverse momentum (bottom). ϵ is varied logarithmically between 10^{-9} and 10^{-5} .

the very soft/collinear radiation. Similarly, the second photon k_T is well-described down to 10 MeV by the choice $\delta = 10^{-4}$ and any smaller values.

However, at 500 GeV, the variation of these radiative observables with the choice of δ is larger. In particular, we see that $\delta = 10^{-7}$ no longer agrees with 10^{-6} , and in fact deviates from the established pattern for harder radiation even than $\delta = 10^{-3}$. This is evidence that a ratio $\delta/\epsilon = 10$ is insufficient for good rescaling of the structure function at this energy, even using the linear method. For this reason, the ratio plots for $\sqrt{s} = 500$ GeV are shown with respect to $\delta = 10^{-6}$.

Focusing on the 0-to-1 jet rate, we find that $\delta = 10^{-4}$ gives a good description of the spectrum down to a transverse-momentum-equivalent value of 30 MeV. The description of the second photon transverse momentum is of lower quality for both collider energies, but the gain in shower speed is significant enough to accept deviations on the order of 10% in the description of the second hardest photon (and only when this is particularly soft). A computational speedup allows the production of higher-quality results overall for the same compute time, hence allowing the better description of more relevant physical effects. As a result, we choose $\delta = 10^{-4}$ for the remainder of this paper.

3.2 Validating the MC@NLO implementation of the shower

To validate the implementation of the MC@NLO method as compared to the standard parton shower, we set $\tilde{V} = -\sum I^S$ and neglect $D^A - D^S$, and expect that the \mathbb{S} -event contribution is exactly equal to the LO standard shower contribution. Fig. 6 shows that they agree at the per-mille level for the Born-level observable $m_{\nu\bar{\nu}}$, the neutrino-pair invariant mass. For the 0-to-1 jet rate, the agreement is 0.1% when we study the process at 91 GeV, and at the same level for 500 GeV for $d_{01} > 10^{-3}$ GeV². Noting that there is a 1% difference between LO+PS and the modified- \mathbb{S} at the extremely soft end of the d_{01} spectrum, this study allows us to quantify the impact of cases where the overestimate described in Sec. 2.2 fails to overestimate the splitting function and the splitting then occurs. When this happens, the MC@NLO shower overweights the event, while the LO shower does not. The effect shown will have no meaningful physical effect and as such we conclude that the overestimate is sufficient for our purpose.

We also study the full MC@NLO contribution and compare it to the LO parton shower prediction and the fixed-order NLO prediction. The total LO cross section is 0.837 pb and the NLO cross section is 0.828 pb: a K -factor of -1%. We find a scheme uncertainty, associated with the choice of mixed α scheme described in Sec. 2.5, of 0.3% on the total cross section for both fixed-order NLO and MC@NLO, based on the difference between the pure G_μ scheme cross section and that obtained with the mixed scheme. We find that the total cross section generated by the MC@NLO method agrees with the NLO one well within this scheme uncertainty, and show the associated distributions in Fig. 7.

For clarity, as well as the total MC@NLO result, we also show the composition of the MC@NLO prediction in terms of the \mathbb{S} -events and \mathbb{H} -events in the lower ratio plot of each subfigure. We find that the \mathbb{S} -events are positive definite or zero for all observables, whilst the \mathbb{H} -events contribute negatively in some regions of phase space.

It is important to note that the initial-state parton shower does not change the final-state invariant mass by construction, due to the kinematic scheme [32]. The top-left subfigure shows the neutrino-pair invariant mass and its ratio to the NLO and LO predictions. From the upper ratio plot it is clear that the MC@NLO and fixed-order NLO agree perfectly across the spectrum. We also observe that the LO and LO+PS predictions lie on top of one another, illustrating the same effect at LO. We find that the effect of including NLO effects, on top of the LL structure function, is to shift the prediction towards lower $m_{\nu\bar{\nu}}$, as expected.

In contrast, in the top right plot of Fig. 7 we show the (matter) neutrino transverse momentum, which is sensitive to the effects of a parton shower if hard emissions are kinematically allowed. We see that the LO, NLO, parton shower and MC@NLO curves are all consistent at small neutrino k_T but that the shower has a sizeable effect on the neutrino transverse momentum above $m_Z/2$, especially at LO where the effect is tens of percent. On the other hand, compared to fixed-order NLO, the MC@NLO correction is much smaller, of the order of 6%. In the case of MC@NLO, we see that both the \mathbb{S} -events and \mathbb{H} -events are positive and non-negligible across the whole spectrum for this observable.

In the middle row of Fig. 7, we study radiative observables: the 0-to-1 jet rate (left) and the transverse momentum of the hardest photon. Here we see the effect of the definition of D^A in our version of the MC@NLO method, see Eq. (2.33), and the scale choice of $\mu_Q^2 = m_{\nu\bar{\nu}}^2$ very clearly. The hard-emission tail of both plots is dominated by the MC@NLO \mathbb{H} -events and the real-emission matrix element R, while the

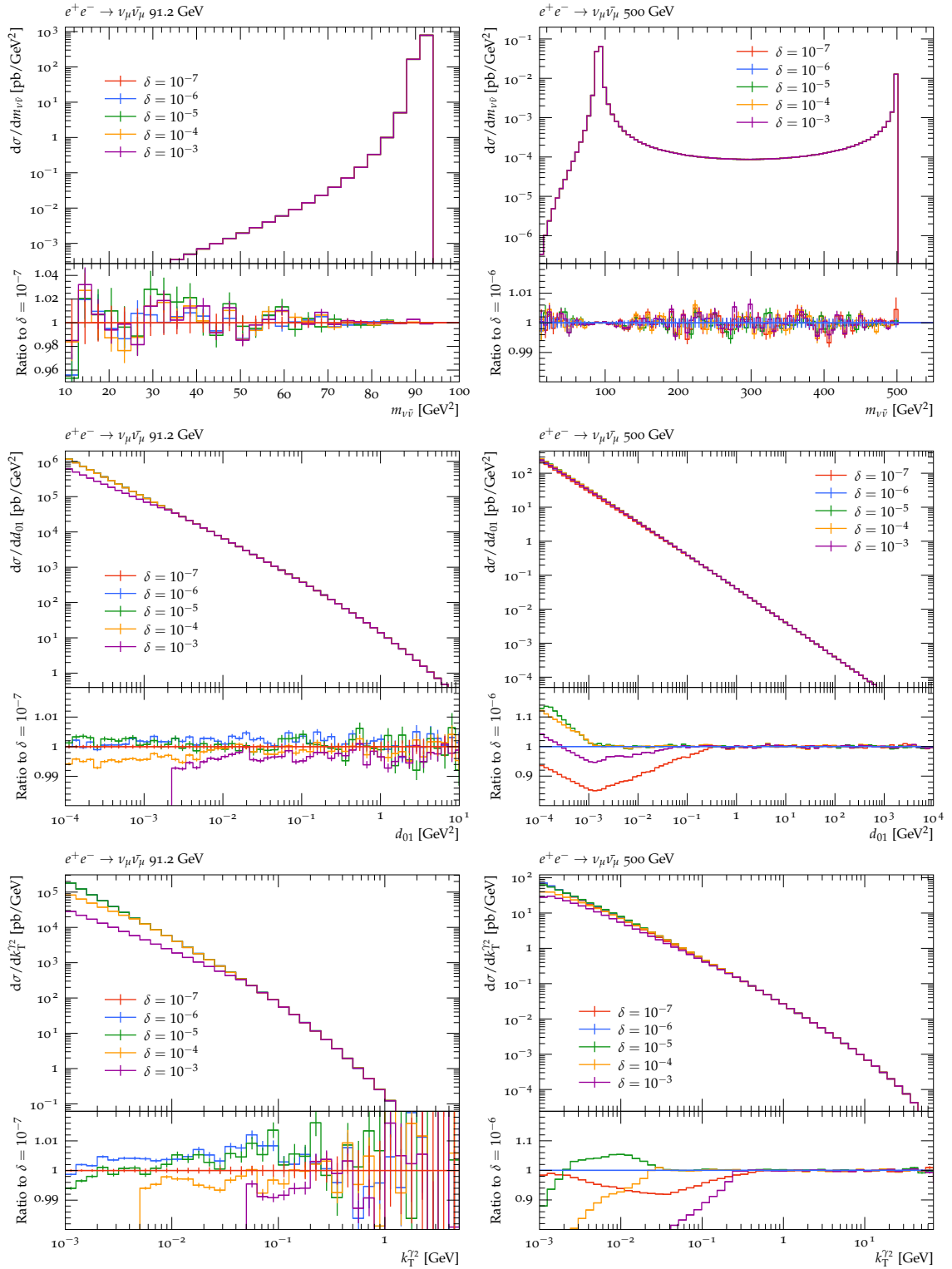


Figure 5: Plots showing the effect of varying the structure function δ parameter for the process $e^+e^- \rightarrow \nu_\mu\bar{\nu}_\mu$ at two different collider energies, 91.2 GeV (left) and 500 GeV (right). The observables shown are the neutrino-pair invariant mass (top row), the 0-to-1 jet rate (middle) and the second photon transverse momentum (bottom). δ is varied logarithmically between 10^{-7} and 10^{-3} . For 91.2 GeV, the ratio is given with respect to $\delta = 10^{-7}$ while for 500 GeV, $\delta = 10^{-6}$ is used as the reference.

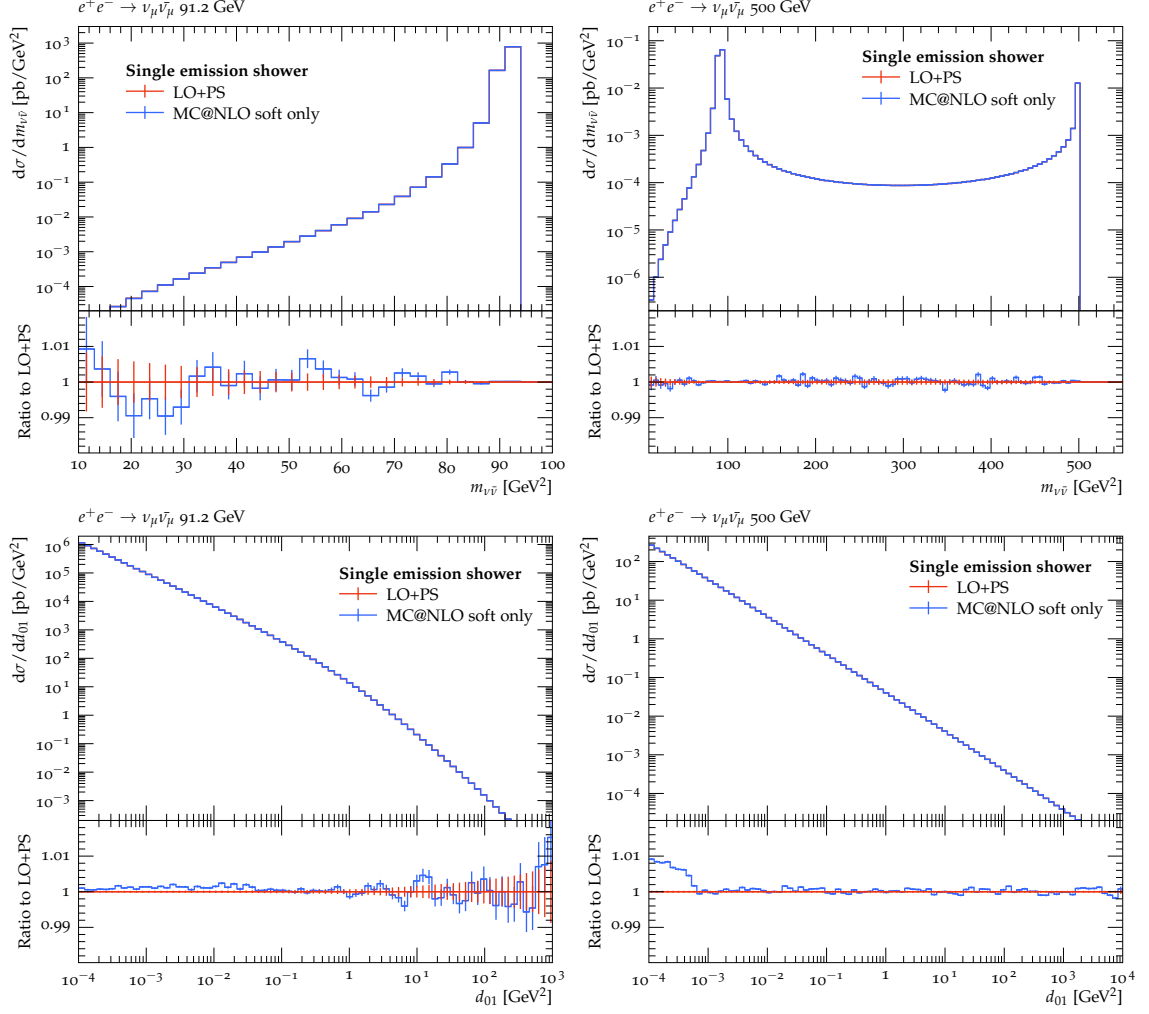


Figure 6: MC@NLO without hard NLO corrections (see main text for details), compared with the LO parton shower prediction, for the process $e^+e^- \rightarrow \nu_\mu\bar{\nu}_\mu$ at two different collider energies, 91.2 GeV (left) and 500 GeV (right). The observables shown are the neutrino-pair invariant mass (top) and the 0-to-1 jet rate (bottom). To illustrate the agreement, only one shower emission is allowed, since further emissions are described by the standard parton shower in both cases.

\mathbb{S} -events dominate at lower k_T . The transition between the \mathbb{S} -events and the \mathbb{H} -events is gradual in general, since it is determined event-by-event using the kinematic scale μ_Q^2 , but in this case the presence of the Z resonance means that μ_Q is highly peaked around the Z mass. Therefore, above m_Z there is an abrupt shift from a small and negative \mathbb{H} -event contribution to a large positive one, since the parton shower kernels are switched off. We see that the LO shower does not describe the spectrum in this region, while the MC@NLO curve agrees, within a percent or so, with the fixed-order NLO one. We see that similarly to a QCD shower, the introduction of a properly-matched parton shower to the NLO prediction leads to a levelling-off of the divergent soft end of the radiation spectrum, but in QED, the position in k_T of the Sudakov peak is much lower than for QCD [70] because of weaker logarithms due to the smaller coupling. A similar, but much smoother, scale-dependent transition between \mathbb{S} - and \mathbb{H} -events is visible in the second-hardest photon k_T distribution (bottom left). This observable is described only at leading-logarithmic accuracy by both the standard shower and MC@NLO, but differences are still seen due to the different kinematics of the \mathbb{S} - and \mathbb{H} -events, both of which undergo standard showering.

Finally, the photon multiplicity (bottom right) shows the cross section differential in the number of photons with transverse momentum above a cut p_T^{min} , here 0.5 GeV. This observable differs only in a constant factor for $N_\gamma > 0$ between LO+PS, \mathbb{S} -events and the full MC@NLO. The fixed-order NLO prediction has fewer unresolved-emission events than the showered predictions. The correction to the zero-photon bin from the \mathbb{H} -events is small, since, by definition, below the 0.5 GeV cut the parton shower describes the real-emission matrix element very well. In all resummed predictions, each extra photon occurs with a frequency of around an order of magnitude less than the previous, consistent with a factor proportional to $\alpha \log(s/(p_T^{\text{min}})^2)$.

4 ZH production at a future e^+e^- collider

The FCC-ee proposal sets forth the production of 2.2×10^6 ZH events at $\sqrt{s} = 240$ GeV with 10.8 ab^{-1} of integrated luminosity [1]. Since the threshold for production of the on-shell ZH state is approximately 216 GeV, there is somewhat restricted phase space for hard quasi-collinear radiation in these events. In this regime, the fixed-order correction is the most important hard radiation correction, and the structure function takes care of the soft and purely collinear radiation. However, 3.7×10^5 ZH events are expected during the 2.70 ab^{-1} run above the $t\bar{t}$ threshold at 365 GeV. At this energy, there can be a large contribution from hard quasi-collinear radiation as well as multiple semi-hard photons. Therefore, we expect that the parton shower contribution, separately from the NLO correction, will be important at this higher energy and many observables will not be fully described by the structure function alone.

We produce on-shell ZH at NLO EW using the setup outlined in Sec. 3, but set the widths of all unstable particles to zero as they now occur as asymptotic states in our calculation. We continue to use the mixed α scheme outlined in section 2.5. For both the fixed-order and the showered predictions, we use the electron structure function, Eq. (2.18), linearly rescaled near the singularity with $\epsilon = 10^{-8}$ and $\delta = 10^{-4}$. For the parton shower infrared cutoff we set $t_c = 10^{-4} \text{ GeV}^2$ for $\sqrt{s} = 240$ GeV and $t_c = 10^{-3} \text{ GeV}^2$ for $\sqrt{s} = 365$ GeV. As before, we restrict the parton shower to allow only photon emissions, to isolate their dominant effect on the relevant observables. The decays of the Z and Higgs can be included using the standard SHERPA decay module [71]. Nominally, QED corrections to these decays are accounted for using the YFS soft-photon resummation [20, 72] properly accounting for resonance shapes [73, 31], while QCD corrections are effected through the standard QCD parton shower [32]. A completely off-shell treatment of intermediate resonances, e.g. in a off-shell $e^+e^- \rightarrow \mu^+\mu^-b\bar{b}$ calculation, is easily possible at the fixed-order level at LO and NLO EW, but the matching to a QED parton shower necessitates a resonance-aware shower spectator assignment to avoid distorting the resonance shapes [74].

4.1 Threshold production: 240 GeV

We begin our discussing of ZH production by investigating the properties of our implementation in threshold production. In Fig. 8 we show the EW MC@NLO prediction for this process, the LO prediction with and without the QED parton shower, and the fixed-order NLO EW prediction. The observables have been chosen reminiscent of those used in the test case of neutrino production, but with a view to including relevant experimental quantities. For example, the ZH final state is typically reconstructed from its decay products, and this combined final state is then studied. Here we have shown predictions for the invariant mass of the ZH system and its overall transverse momentum k_T^{ZH} , in addition to the Z transverse momentum. It is

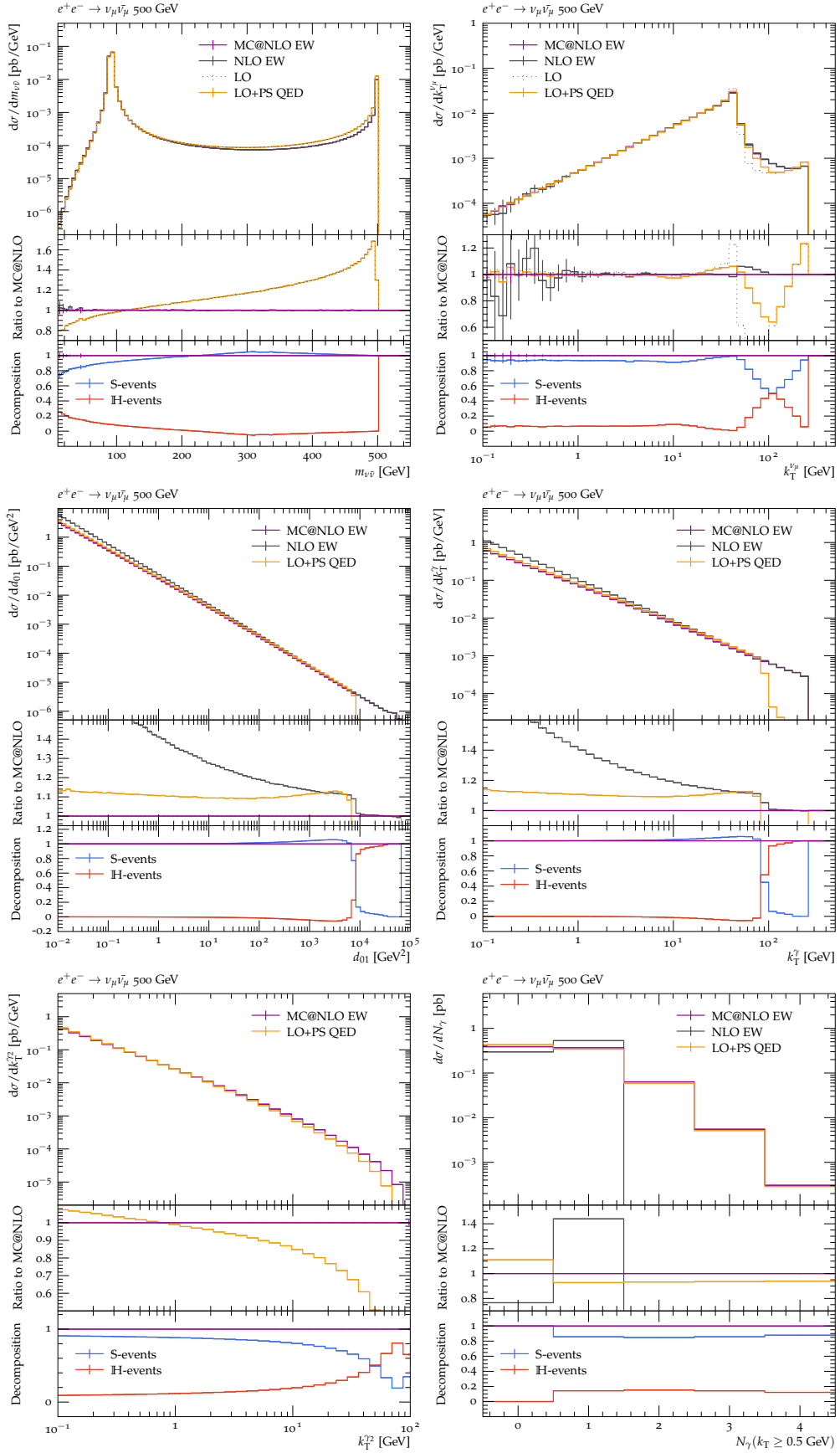


Figure 7: A comparison of MC@NLO, the fixed-order NLO prediction and the leading-order prediction with and without the parton shower for the process $e^+e^- \rightarrow \nu_\mu \bar{\nu}_\mu$ at 500 GeV. The lower ratio plot in each subfigure shows the composition of the MC@NLO prediction in terms of the S- and H-events.

clear from kinematic constraints that the latter is highly correlated with the Higgs transverse momentum, and that the ZH transverse momentum is highly correlated with that of the hardest photon.

The ZH invariant mass (top left subfigure of Fig. 8) shows, as before, that the resummed predictions reproduce the fixed-order ones, at their respective order, to sub-percent precision. While the correction to the total cross section is -24%, the local NLO K -factor rises to about -40% just below \sqrt{s} before decreasing again to -25%, showing the importance of higher EW perturbative accuracy for this observable and in turn implying that the NNLO correction will be an important inclusion. This shape is exactly reproduced by our MC@NLO computation.

In the top-right plot we show the Z transverse momentum, plotted logarithmically from 1 GeV up to the kinematic limit. Whilst the initial-state parton shower can in principle change the distribution in this observable, we find that the effect is very small due to the lack of phase space for hard collinear radiation, both at LO and NLO. This is in contrast to the case of neutrino production, where the neutrino k_T received sizeable corrections from the inclusion of parton shower effects. The lower ratio plot shows that the NLO correction is almost flat in this observable, again in contrast to high-energy neutrino production.

We show radiative observables on the middle row of Fig. 8. It can be seen that the transverse recoil of the ZH final state (middle right) is very highly correlated with the 0-to-1 jet rate (middle left) under these conditions. Again, it is important to note that like the invariant mass, these observables, which vanish at Born level, will be changed significantly by final-state radiation, and are thus described incompletely, serving only to quantify the initial-state radiation which is our focus here.

It is clear that the parton shower approximation is a large overestimate of the photon-emission matrix element R , as seen in the comparison of the LO+PS jet rate compared with the NLO prediction. The MC@NLO prediction lies lower still as a result of the negative virtual amplitude, which contributes to radiative observables due to the action of the parton shower, in contrast to the fixed-order case. Unlike for neutrino production in which the parton shower starting scale was primarily identified with $t_n = m_{\nu\nu}^2 \approx m_Z^2$, there is no dominant scale identification for the parton shower starting scale $t_n = m_{ZH}^2$ in this process, hence there is no region in which the S-events do not contribute. Truncated at relative $\mathcal{O}(\alpha)$, the NLO and MC@NLO predictions agree for large k_T^{ZH} as shown in Sec. 2.3, but it is clear from the plot that higher-order contributions are of the order of 20% for these observables, inline with the inclusive corrections. These originate from the smoothing behaviour of MC@NLO, in which virtual corrections are present within the radiative phase space, but this behaviour is of $\mathcal{O}(\alpha^2)$ and can only be constrained by a dedicated NNLO calculation.

We also show the properties of the resummation in MC@NLO using the second-hardest photon transverse momentum, $k_T^{\gamma_2}$ in the lower left plot of Fig. 8. For this observable, the MC@NLO correction compared to LO+PS is very large and negative, around 50% even for hard photons and greater than a factor of 2 for soft photons. Both the LO and MC@NLO predictions are less than leading-order in this observable—only the resummed terms contribute—but in MC@NLO these are resummed on top of the \bar{B} matrix element, in contrast to LO+PS.

Finally, the photon multiplicity is shown in the bottom-right plot. Unlike for neutrino production at 500 GeV, we see fewer than 1 per million events contain four or more non-soft photons. The expected logarithmic decrease in $d\sigma/dN_\gamma$ in increasing N_γ is amplified here by an additional drop due to kinematic constraints. Nevertheless, we find the expected relative 0- and 1-bin contributions at NLO and in MC@NLO. We also see that the ratio between the LO+PS and MC@NLO predictions flattens out from the 2-photon bin onwards, since both are determined by the same standard QED parton shower.

4.2 Radiative production: 365 GeV

We now investigate the changes in the description of ZH brought about by the increased phase space available for QED radiation when the centre-of-mass energy of the collision is increased. To this end, in Fig. 9, we show the set of observables defined above for the $\sqrt{s} = 365$ GeV $e^+e^- \rightarrow ZH$ process. As for 240 GeV, the NLO and MC@NLO predictions for the total cross section and the ZH invariant mass agree within 0.5%, as expected. The NLO EW correction to the total cross section is -23%.

Studying the effect of the parton shower on the LO prediction, we see from the top right plot of Fig. 9 that the parton shower decreases the Z transverse momentum distribution by up to 2%. Whilst one might expect that a similar deviation would be seen at NLO, the effect is instead much smaller, illustrating that the dominant radiative effect on k_T^Z is captured at NLO and that effects beyond NLO are small for this

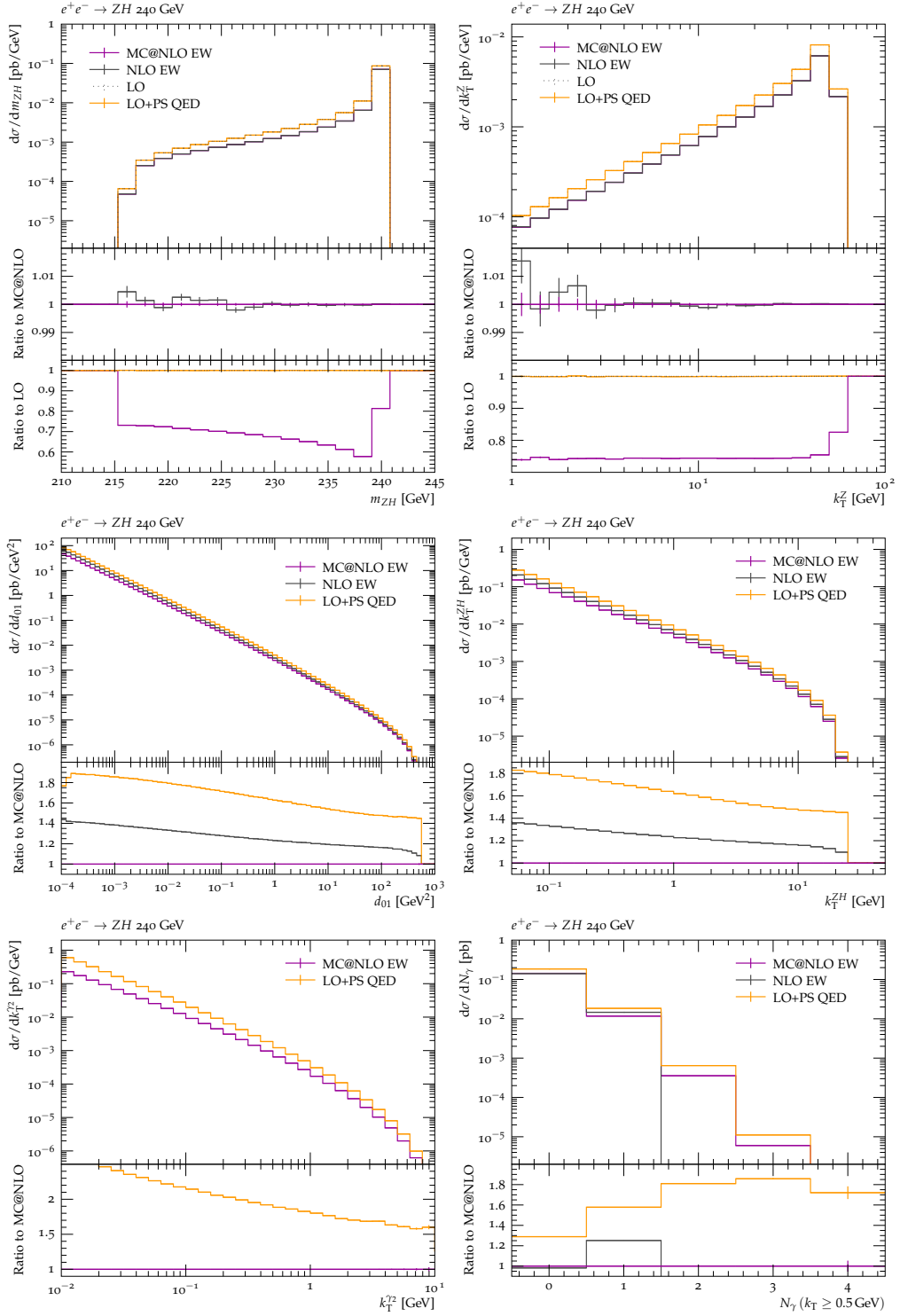


Figure 8: A comparison of MC@NLO, the fixed-order NLO prediction and the leading-order prediction with and without the parton shower for the process $e^+e^- \rightarrow ZH$ at 240 GeV.

observable.

By looking at the radiative plots (middle row), we see that LO+PS overestimates the hard radiation particularly severely at this energy, an effect of over 80% compared to MC@NLO, whereas the effect at 240 GeV was 40%. Since the MC@NLO does not suffer from this shape difference, and is roughly flat with respect to the fixed-order NLO for hard radiation, the effect of the two calculations yields an almost equivalent k_T^Z distribution. We also see that similarly to the 240 GeV case, the MC@NLO prediction lies below the fixed-order NLO one across the whole spectrum. Since the total cross section is the same, this implies that MC@NLO produces a larger cross section with a Born kinematical configuration than an NLO prediction does. This is backed up by the photon multiplicity (bottom right), where the fixed-order prediction is 6% lower in the zero-photon bin than MC@NLO. As for 240 GeV, the H-event contribution in the radiative observables is to correct the parton shower's region of poor approximation in hard radiation. Again, there is no region in which the S-events do not contribute, and as such the MC@NLO and NLO predictions do not exactly agree even for hard radiation due to effects beyond NLO.

We can see from the lower left plot of Fig. 9 that the MC@NLO method produces a second-photon transverse momentum distribution which is flat over a large range of transverse momenta with respect to the standard parton shower. This pattern is repeated for further photons, as can be seen in the ratio plot for the N_γ distribution. The differences in the second photon k_T shape, and the large deviations from a constant ratio in the zero- and one-photon bins in multiplicity, are due to the different underlying matrix elements in the LO+PS and MC@NLO methods.

It is interesting to note that despite the $\sqrt{s} = 240$ GeV and 365 GeV setups allowing for different radiation patterns in principle, the shapes of all NLO predictions for the observables studied here are very similar between the two different centre-of-mass energies. The higher centre-of-mass energy ultimately results in an extension of the invariant mass peak seen in Fig. 8 (top left) to a sharper peak at the higher energy. This increases the size of the parton shower correction at LO, but at NLO clearly the dominant hard collinear radiation is already present in the fixed-order NLO prediction (both from the matrix element and from the structure function). This suggests that if exclusive description of multiple photons and generation of unweighted events is not required, it is sufficient to consider NLO with a structure function at this accuracy. Nonetheless, the features of MC@NLO are desirable in a wide range of processes.

The presence of phase-space cuts will also affect this assessment. While a structure function can appropriately shift the momenta of the initial-state leptons to capture the radiative return phenomenon, only a QED parton shower (matched to NLO) adequately describes the transverse boost which a final state may acquire due to initial-state non-collinear radiation. In the analyses presented here, we have been inclusive of such boosts, but in general the effect on observables will be non-trivial due to selection cuts.

5 Conclusions

In this paper we have presented the first automated matching of a QED parton shower and an NLO EW calculation for lepton colliders. In particular, the results shown here constitute the first MC@NLO EW prediction for ZH production at proposed working points at a future electron-positron collider, including the full NLO EW corrections as well as the leading-logarithmic corrections from the QED parton shower. The method is general and, in its current form, is easily applicable to all processes for which initial-final interference beyond NLO is suppressed and which do not contain a combination of tagged (resolved) and untagged (unresolved) photons at leading order. Even considering these caveats, this includes a majority of colourless processes at current and future electron-positron colliders. To describe coloured final states, or for processes at hadron colliders, the combined QCD+EW matched interleaved parton shower is a straightforward extension of the methods presented here. At low energies where perturbative QCD is not applicable, various phenomenological models for describing hadronic cross sections can be combined with the QED parton shower, and the matching proceeds similarly. In particular, the methods presented here are highly applicable to the description of low-energy electron-positron collisions, both for the energy scan and radiative return methods. Bhabha scattering requires an excellent description of initial-final interference, but di-muon and di-pion production (and their radiative analogues) can be considered either in the presence or absence of this interference. The study of these processes will be the subject of future work.

The QED parton shower and the associated MC@NLO EW have each undergone stringent validation testing, detailed in section 3. To validate the methods, we have varied the parameters which control infrared limits

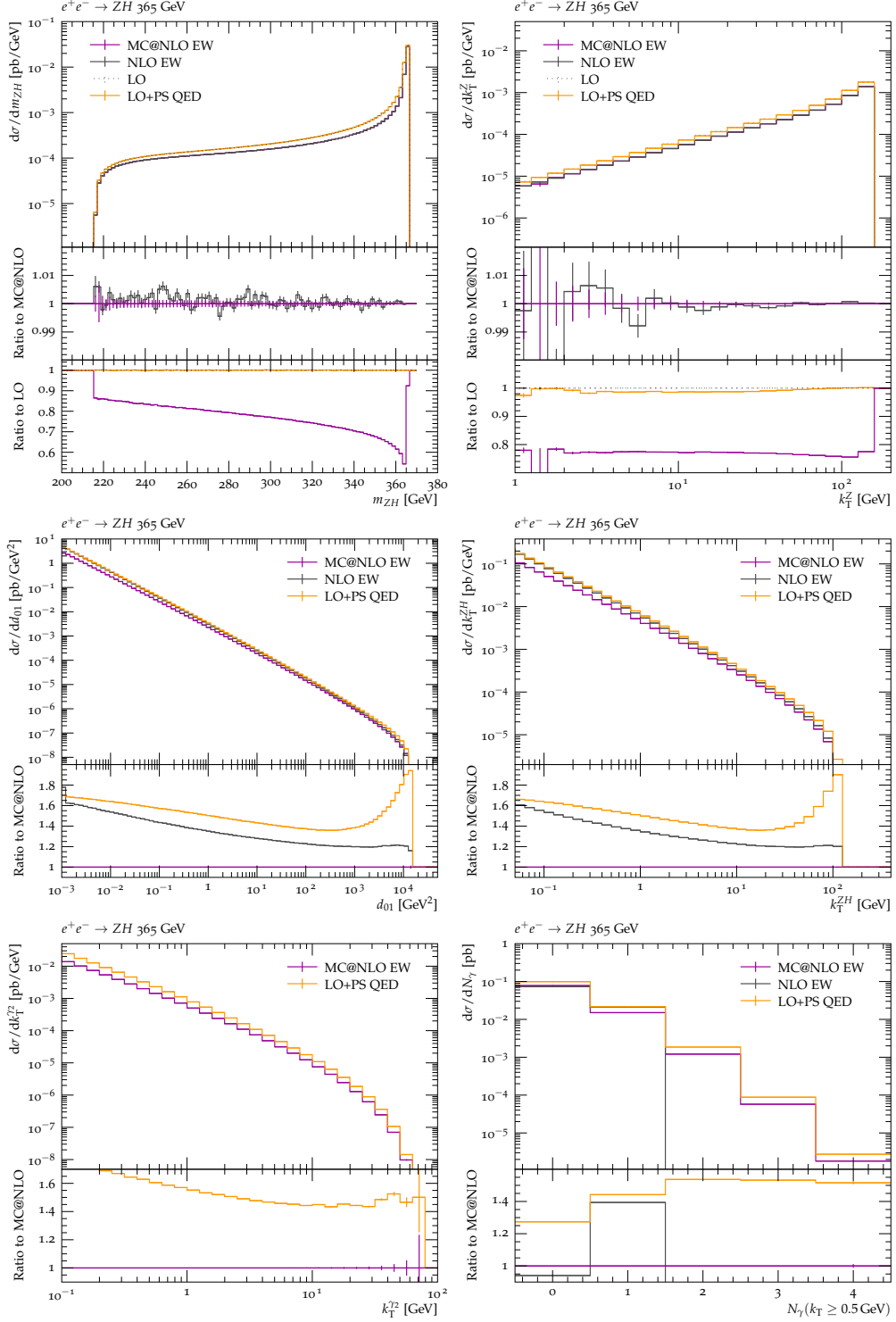


Figure 9: A comparison of MC@NLO, the fixed-order NLO prediction and the leading-order prediction with and without the parton shower for the process $e^+e^- \rightarrow ZH$ at 365 GeV.

of different parts of the calculation, verified that they do not change Born-level observables and that their impact on radiative observables is predictable and small. Based on these studies, we have chosen an optimal set of parameters for a future collider setup. In general, we expect that the optimal parameter choices will depend on the order of magnitude of the centre-of-mass energy, as well as the observables under consideration and fiducial cuts.

The main results which we have used to illustrate the predictions of the method are for the ZH production process at a future e^+e^- collider such as the FCC-ee. We have shown how the MC@NLO method reproduces the fixed-order accuracy for the total cross section, the final-state invariant mass and the Z boson transverse momentum; and that it models soft and collinear radiation beyond NLO according to the parton shower approximation. In particular, there is a smooth transition between these regions owing to the construction of the method and the choice of scales.

A key part of the method presented here is the automated identification of n -parton configurations, and the scales associated with these, in order to correctly identify a hardest emission in each event and to set the shower starting scale accordingly. This ensures the respective accuracy of the NLO correction and the resummation. We have achieved this identification using a QED-flavour-aware version of SHERPA’s MEPS scale setter. In complement to this, when analysing the results, we used a flavour-aware jet clustering algorithm to quantify the behaviour of the parton shower.

In addition to the work directly on the MC@NLO and parton shower, it was necessary to modify the way that the electron structure function is conventionally modelled in event generators. Due to the parton shower’s rescaling of initial-state momenta, the traditional choice of rescaling the structure function near the $x \rightarrow 1$ integrable singularity was not suitable for the LO parton shower, let alone for the MC@NLO method. In this paper we have introduced a linear rescaling, which keeps the structure function continuous until its numerical cutoff, and a graduated shower cutoff x_{max} . This means that the parton shower can emit into the rescaled region, but is then forbidden from acting again on that initial-state particle. Ideally, however, the rescaling used would render the structure function differentiable in the domain $[0, 1 - \epsilon)$. For this purpose, we are considering sigmoid weighting functions.

Throughout this paper, we have used an electron structure function which is derived starting from LO evolution kernels (the Altarelli-Parisi functions) using LO initial conditions, $f_e(x, m_e^2) = \delta(1 - x)$. To go beyond this approximation, one can produce a next-to-leading logarithmic structure function [49, 75, 76, 50, 51]. This entails using NLO initial conditions, which preclude neglecting the photonic initial state as we have done here. A future plan for the QED parton shower in SHERPA is to allow for the evolution starting from a NLL structure function, or indeed from a full parton distribution function, in analogy with QCD. Lepton PDFs suitable for use in an event generator are still under development, but are expected in the near future.

All analyses and plots were made using RIVET [77, 78, 79].

Acknowledgements

The authors would like to thank Alan Price, Carlo Carloni Calame, and Stefan Dittmaier for helpful discussions. Joanne Roper’s careful reading of the manuscript is hugely appreciated. MS is funded by the Royal Society through a University Research Fellowship (URF\R\231031 and URF\R1\180549) and Enhancement Awards (RF\ERE\210397, RGF\EA\181033 and CEC19\100349). LF is supported by the Leverhulme Trust, LIP-2021-014. LF also acknowledges support from an STFC studentship under the STFC training grant ST/P001246/1 for the early parts of this work.

A KP terms in the presence of lepton structure functions

This appendix details modifications to the Catani-Seymour subtraction of QED singularities [28, 29, 30] necessary to be used in conjunction with lepton PDFs, namely the \mathbf{K} and \mathbf{P} operators in particular. As a first observation, while the \mathbf{K} operator contains a factorisation-scheme dependent contribution, any scheme dependence vanishes to LL accuracy [80] and does not have to be considered in the present work. This leaves us to deal with the numerical instabilities induced by the integrable singularity at $z = 1$ in the electron structure function, see Sec. 2.2. Following the notation of [30], the \mathbf{K} and \mathbf{P} operator contributions to an

arbitrary IR-safe observable O for beam A can be expressed in the following form

$$\langle O \rangle_{\mathbf{KP}}^A = \sum_{a,b} \int d\eta_a d\eta_b \int d\Phi_m \sum_{a'} \int_0^1 dx_a \mathbf{B}_{a'b}(x_a \eta_a, \eta_b; \Phi_m) \left[\mathbf{K}_{aa'}(x_a; \{\alpha_{\text{dip}}\}) + \mathbf{P}_{aa'}(x_a; \mu_F^2) \right] O(\Phi_m) \quad (\text{A.1})$$

where a and b would run over all possible partonic initial states, although when using the usual electron structure functions, $a, b \in \{e^+\}$ or $\{e^-\}$ only, depending on the beam. η_a and η_b are their momentum fractions. Likewise, a' would run over all possible partonic initial states, but is restricted to $\{e^+\}$ or $\{e^-\}$, respectively. The hard scattering process is defined as $\mathbf{B}_{ab} = f_a f_b \mathcal{B}_{ab}$ to include the parton densities f_a and f_b , and the partonic cross section \mathcal{B}_{ab} . $x_a \eta_a$ is then the remaining momentum fraction of flavour a' after the integrated-over emissions $a \rightarrow a' + X$, which enters the hard scattering. The \mathbf{K} and \mathbf{P} operators, resulting from the combination of the integrated subtraction terms and the collinear counterterms, depend on the additional x integration variable as [81, 30]

$$[g(x)]_+ + \delta(1-x)h(x) + k(x).$$

Thus, using the definitions of the plus prescription and δ -function,

$$\begin{aligned} \langle O \rangle_{\mathbf{KP}}^A &= \sum_{a,b} \int d\eta_a d\eta_b \int d\Phi_m \mathbf{B}_{ab}(\eta_a, \eta_b; \Phi_m) \\ &\times \sum_{a'} \left\{ \int_{\eta_a}^1 dx_a \left[\frac{f_{a'}\left(\frac{\eta_a}{x_a}\right)}{x_a f_a(\eta_a)} \left(g^{aa'}(x_a) + k^{aa'}(x_a) \right) - \frac{f_{a'}(\eta_a)}{f_a(\eta_a)} g^{aa'}(x_a) \right] \right. \\ &\quad \left. + \frac{f_{a'}(\eta_a)}{f_a(\eta_a)} \left(h^{aa'} - G^{aa'}(\eta_a) \right) \right\} O(\Phi_m), \end{aligned} \quad (\text{A.2})$$

where, after factorising out the $x_a = 1$ piece of the hard scattering process, we have split the x_a integration into two regions: $x_a \in (0, \eta_a)$ and $x_a \in (\eta_a, 1)$. Integrating the remaining piece using $f_a(z) = 0$ for $z > 1$ and defining $G^{aa'}(\eta) = \int_0^\eta dx g^{aa'}(x)$ and $h^{aa'} \equiv h^{aa'}(1)$. When using electron structure functions, i.e. $a, a' \in \{e^+\}$ and $b \in \{e^-\}$ only (and the reverse which follows trivially), and wanting to execute the remaining integration over x_a numerically, this form still suffers from the integrable singularity of $f_e(z)$ as $z \rightarrow 1$. We thus again introduce an ε -environment, with $\varepsilon \ll 1$, to split the integration region into two domains, $[\eta_a, \eta_a/(1-\varepsilon)]$ and $[\eta_a/(1-\varepsilon), 1]$,

$$\begin{aligned} \langle O \rangle_{\mathbf{KP}}^A &\equiv \langle O \rangle_{\mathbf{KP}}^A|_{(\varepsilon=0)} \\ &= \sum_{a,b} \int d\eta_a d\eta_b \int d\Phi_m \mathbf{B}_{ab}(\eta_a, \eta_b; \Phi_m) \\ &\times \sum_{a'} \left\{ \int_{\frac{\eta_a}{1-\varepsilon}}^1 dx_a \left[\frac{f_{a'}\left(\frac{\eta_a}{x_a}\right)}{x_a f_a(\eta_a)} \left(g^{aa'}(x_a) + k^{aa'}(x_a) \right) - \frac{f_{a'}(\eta_a)}{f_a(\eta_a)} g^{aa'}(x_a) \right] \right. \\ &\quad \left. + \frac{f_{a'}(\eta_a)}{f_a(\eta_a)} \left(h^{aa'} - G^{aa'}(\eta_a) \right) \right\}_{\varepsilon=0} O(\Phi_m) \\ &= \langle O \rangle_{\mathbf{KP}}^A|_\varepsilon + \sum_{a,b} \int d\eta_a d\eta_b \int d\Phi_m \mathbf{B}_{ab}(\eta_a, \eta_b; \Phi_m) \\ &\quad \times \sum_{a'} \left\{ \frac{g^{aa'}(\eta_a) + k^{aa'}(\eta_a)}{f_a(\eta_a)} \int_{\eta_a}^{\frac{\eta_a}{1-\varepsilon}} dx_a \left[\frac{1}{x_a} f_{a'}\left(\frac{\eta_a}{x_a}\right) \right] - \frac{f_{a'}(\eta_a)}{f_a(\eta_a)} \frac{\varepsilon \eta_a}{1-\varepsilon} g^{aa'}(\eta_a) \right\} O(\Phi_m). \end{aligned} \quad (\text{A.3})$$

While the x_a integration can still be performed numerically on the $[\eta_a/(1-\varepsilon), 1]$ domain, giving $\langle O \rangle_{\mathbf{KP}}^A|_\varepsilon$, both $g^{aa'}(x_a)$ and $k^{aa'}(x_a)$ are sufficiently well behaved so we can integrate the remaining piece on the small

| | y | z | | y | z |
|----|--|-------------------------------------|----|-------------------------------------|---|
| FF | $\frac{p_i p_j}{p_i p_j + p_i p_k + p_j p_k}$ | $\frac{p_i p_k}{p_i p_k + p_j p_k}$ | IF | $\frac{p_a p_j}{p_a p_j + p_a p_k}$ | $\frac{p_a p_j + p_a p_k - p_j p_k}{p_a p_j + p_a p_k}$ |
| FI | $\frac{p_i p_j - 2(m_{\tilde{\nu}_j}^2 - m_i^2 - m_j^2)}{p_j p_a + p_i p_a}$ | $\frac{p_i p_a}{p_i p_a + p_j p_a}$ | II | $\frac{p_j p_a}{p_a p_b}$ | $\frac{p_a p_b - p_j p_a - p_j p_b}{p_a p_b}$ |

Table 3: Definitions of the dipole variables y and z for all four dipole configurations.

ε -environment analytically. For $a = a' = e$, using the asymptotic form of the electron structure function of Eq. (2.19) and introducing a change of variables $\frac{\eta}{x} = 1 - \xi$, the integral over the structure function simplifies to

$$\int_{\frac{\eta}{1-\varepsilon}}^{\frac{\eta}{\varepsilon}} \frac{dx}{x} f_e\left(\frac{\eta}{x}\right) \xrightarrow{\frac{\eta}{x} \rightarrow 1} \beta \int_0^{\varepsilon} \frac{d\xi \xi^{\beta-1}}{1-\xi} \xrightarrow{\varepsilon \rightarrow 0} \varepsilon^{\beta}. \quad (\text{A.4})$$

This gives us the final expression for the **KP**-terms for the use of the electron structure function at electron-positron colliders,

$$\begin{aligned} \langle O \rangle_{\mathbf{KP}}^{e^+} &= \langle O \rangle_{\mathbf{KP}}^{e^+} \Big|_{(\varepsilon)} + \int d\eta_{e^+} d\eta_{e^-} \int d\Phi_m \mathbf{B}_{e^+e^-}(\eta_{e^+}, \eta_{e^-}; \Phi_m) \\ &\quad \times \left\{ \frac{\varepsilon^{\beta}}{f_{e^+}(\eta_{e^+})} \left(g^{e^+e^+}(\eta_{e^+}) + k^{e^+e^+}(\eta_{e^+}) \right) - \varepsilon \eta_{e^+} g^{e^+e^+}(\eta_{e^+}) \right\} O(\Phi_m). \end{aligned} \quad (\text{A.5})$$

Particular care has to be taken if $\eta_a > 1 - \varepsilon$. In this situation, a redefinition of $\varepsilon \rightarrow \tilde{\varepsilon} = 1 - \eta_a$ is necessary. It remains to choose a value for the regulator ε . While ε must not be too large for our approximation in the analytical integration to hold, a large ε also reduces the number of phase space points for which the numerical integral is evaluated, increasing its Monte-Carlo statistical uncertainty. Likewise, for values of $\varepsilon < \delta$, as it is defined in Sec. 2.2, the reweighting from $f_e \rightarrow W_e$ must not be applied in the numerator PDF ratios from Eq. (A.2) but still in their denominators. However, for MC@NLO, the value of ε impacts the phase-space generation in a broader way, since all Born-type events are generated together. A too-small ε is therefore prohibitively inefficient. For the optimal efficiency, and minimal error, for both fixed-order and MC@NLO we thus choose $\varepsilon = 10^{-3}$.

B Splitting functions

In this appendix we detail the splitting functions used in the QED parton shower and MC@NLO. To describe the QED splitting functions, we will need to introduce the U(1) analogue to the colour correlator, the charge correlator [20, 47, 48, 31, 30], defined as

$$\mathbf{Q}_{\tilde{\nu}_j \tilde{k}}^2 = \begin{cases} \frac{Q_{\tilde{\nu}_j} \theta_{\tilde{\nu}_j} Q_{\tilde{k}} \theta_{\tilde{k}}}{Q_{\tilde{\nu}_j}^2} & \text{for } \tilde{\nu}_j \neq \gamma \\ \kappa_{\tilde{\nu}_j \tilde{k}} & \text{for } \tilde{\nu}_j = \gamma \end{cases} \quad \text{with} \quad \sum_{\tilde{k} \neq \tilde{\nu}_j} \kappa_{\tilde{\nu}_j \tilde{k}} = -1 \quad \forall \tilde{\nu}_j = \gamma, \quad (\text{B.1})$$

where the $Q_{\tilde{\nu}_j}$ and $Q_{\tilde{k}}$ are the charges of the emitter and spectator and $\theta_{\tilde{\nu}_j/\tilde{k}} = 1(-1)$ if they are the final (initial) state. The $\kappa_{\tilde{\nu}_j \tilde{k}}$ are parameters that can be chosen to implement a spectator-assigning scheme but are subject to the constraint that the sum over all possible spectators adds up to the correct collinear limit. Various choices are implemented, see [30]. Their phenomenological impact has been explored in [69] and found to be minor.

We use the dipole indices illustrated in Fig. 1 in the definitions of the splitting functions and other variables. These differ for each dipole type, and we use the final-final notation for a general dipole.

The general form of the dipole splitting functions is

$$D_{ij,k}^A = -\frac{1}{2p_i p_j} \mathbf{Q}_{\tilde{\nu}_j \tilde{k}}^2 \langle \dots, \tilde{\nu}_j, \dots, \tilde{k}, \dots | \mathbf{V}_{ij,k} | \dots, \tilde{\nu}_j, \dots, \tilde{k}, \dots \rangle, \quad (\text{B.2})$$

where $|\dots, \tilde{ij}, \dots, \tilde{k}, \dots\rangle$ is a vector in colour and helicity space, and thus the product indicates a squared matrix element, summed over final-state colours and spins.

The parton shower splitting functions are then the spin-averaged forms of $D_{ij,k}^A$, in 4 dimensions, divided by the Born contribution.

$$S_{\tilde{ij}(\tilde{k}) \rightarrow ij(k)} = -\frac{1}{2p_i p_j} \mathbf{Q}_{\tilde{ij}\tilde{k}}^2 \frac{\langle s | \mathbf{V}_{ij,k} | s \rangle |_{\epsilon=0}}{\mathbf{B}}, \quad (\text{B.3})$$

in terms of the splitting variable y and light-cone momentum fraction z . For each dipole type, these variables are defined in table 3. The remaining splitting functions can be obtained by interchanging $i \leftrightarrow j$, and simultaneously $z \leftrightarrow 1 - z$.

Final-final. For a final-state splitter \tilde{ij} and a final-state spectator \tilde{k} ,

$$\begin{aligned} S_{f_{\tilde{ij}(\tilde{k})} \rightarrow f_i \gamma_j(k)} &= S_{\bar{f}_{\tilde{ij}(\tilde{k})} \rightarrow \bar{f}_i \gamma_j(k)} = -\frac{8\pi\alpha}{(p_i + p_j)^2 - m_{\tilde{ij}}^2} \mathbf{Q}_{\tilde{ij}\tilde{k}}^2 \left[\frac{2}{1-z+zy} - \frac{\tilde{v}}{v} \left(1+z + \frac{m_i^2}{p_i p_j} \right) \right] \\ S_{\gamma_{\tilde{ij}(\tilde{k})} \rightarrow f_i \bar{f}_j(k)} &= -\frac{8\pi\alpha}{(p_i + p_j)^2} \mathbf{Q}_{\tilde{ij}\tilde{k}}^2 \left[1 - 2(z(1-z) - z_+ z_-) \right]. \end{aligned} \quad (\text{B.4})$$

The relative velocities v and \tilde{v} are introduced to facilitate the analytic integration for the case of massive partons, and the ratio reduces to unity for massless particles. z_{\pm} are the phase space boundaries. Explicit expressions for these are given in the SHERPA parton shower literature, e.g. ref. [32].

Final-initial. For a final-state splitter \tilde{ij} and a massless initial-state spectator \tilde{a} ,

$$\begin{aligned} S_{f_{\tilde{ij}(\tilde{a})} \rightarrow f_i \gamma_j(a)} &= S_{\bar{f}_{\tilde{ij}(\tilde{a})} \rightarrow \bar{f}_i \gamma_j(a)} = -\frac{8\pi\alpha}{(p_i + p_j)^2 - m_{\tilde{ij}}^2} \frac{1}{y} \mathbf{Q}_{\tilde{ij}\tilde{a}}^2 \left[\frac{2z}{1-z+y} + (1-z) - \frac{m_i^2}{p_i p_j} \right] \\ S_{\gamma_{\tilde{ij}(\tilde{a})} \rightarrow f_i \bar{f}_j(a)} &= -\frac{8\pi\alpha}{(p_i + p_j)^2} \frac{1}{y} \mathbf{Q}_{\tilde{ij}\tilde{a}}^2 \left[1 - 2(z_+ - z)(z - z_-) \right], \end{aligned} \quad (\text{B.5})$$

where as before, y is the splitting variable defined in Tab. 3.

Initial-final. For a massless initial-state splitter $\tilde{a}\tilde{j}$ and a final-state spectator \tilde{k} , the IF splitting functions are

$$\begin{aligned} S_{f_{\tilde{a}\tilde{j}(\tilde{k})} \rightarrow f_a \gamma_j(k)} &= S_{\bar{f}_{\tilde{a}\tilde{j}(\tilde{k})} \rightarrow \bar{f}_a \gamma_j(k)} = -\frac{8\pi\alpha}{2p_a p_j} \frac{1}{z} \mathbf{Q}_{\tilde{a}\tilde{j}\tilde{k}}^2 \left[\frac{2z}{1-z+y} + (1-z) \right] \\ S_{\gamma_{\tilde{a}\tilde{j}(\tilde{k})} \rightarrow f_a \bar{f}_j(k)} &= -\frac{8\pi\alpha}{2p_a p_j} \frac{1}{z} \mathbf{Q}_{\tilde{a}\tilde{j}\tilde{k}}^2 \left[1 - 2z(1-z) \right]. \end{aligned} \quad (\text{B.6})$$

The splitting variables z and y are given in table 3, taking care to note that the dipole labels are different from the FI case, see Fig. 1.

Initial-initial. For a massless initial-state splitter $\tilde{a}\tilde{j}$ and a massless initial-state spectator \tilde{b} ,

$$\begin{aligned} S_{f_{\tilde{a}\tilde{j}(\tilde{b})} \rightarrow f_i \gamma_j(a)} &= S_{\bar{f}_{\tilde{a}\tilde{j}(\tilde{b})} \rightarrow \bar{f}_i \gamma_j(a)} = -\frac{8\pi\alpha}{2p_a p_j} \frac{1}{z} \mathbf{Q}_{\tilde{a}\tilde{j}\tilde{b}}^2 \left[\frac{2(z+y)}{1-z} + (1-z-y) \right] \\ S_{\gamma_{\tilde{a}\tilde{j}(\tilde{b})} \rightarrow f_i \bar{f}_j(a)} &= -\frac{8\pi\alpha}{2p_a p_j} \frac{1}{z} \mathbf{Q}_{\tilde{a}\tilde{j}\tilde{b}}^2 \left[1 - 2(z+y)(1-z-y) \right]. \end{aligned} \quad (\text{B.7})$$

These splitting functions can be extended to take into account massive initial-state particles, provided that the corresponding subtraction is implemented for MC@NLO and that the PDF or structure function, as well as the corresponding quasi-collinear factorisation used, is suitable for use with massive partons [82, 83, 84, 85, 86, 87].

C Usage and settings

In this appendix we list the available settings which steer the calculation of the effects described in this paper. They will be available from a future version of SHERPA 3. All are correct at the time of publication, however, these are subject to change between versions of SHERPA, so the reader is encouraged to consult the appropriate version of the manual.

For the QED parton shower, like the QCD parton shower, the scale setter must be set to `MEPS`. Under the scoped setting `SHOWER`, the following settings can be changed:

`EW_MODE` This setting turns on splitting functions for the QED parton shower.

- 0 no QED splittings (default),
- 1 all QED splittings,
- 3 photon emissions off fermions only.

`QED_FS_PT2MIN` The infrared cutoff in t , the parton shower ordering variable, for the QED final-state evolution. Default is 10^{-8} GeV².

`QED_IS_PT2MIN` The infrared cutoff in t , the parton shower ordering variable, for the QED initial-state evolution. Default is 10^{-6} GeV².

`QED_SPECTATOR_SCHEME` This setting controls which charged particles may act as spectators for the emission of a photon off a fermion.

- `One` only the nearest opposite-sign same flavour particle considered (default),
- `All` all charged external legs in the event considered.

The nearest particle is selected by taking the minimum dipole invariant mass. All charged particles are always considered as spectators for photon splittings and are given equal weight. There is an analogous setting under the `MCATNLO` scope (default : `All`).

`QED_ALLOW_FI` This setting controls whether to allow initial-final interference in the QED shower. Note that if switched on, `QED_SPECTATOR_SCHEME` must be set to `All`.

- `false` no initial-final interference (default),
- `true` initial-final and final-initial dipoles included.

`QED_ALLOW_II` This setting controls whether to allow initial-state particles to participate in the QED parton shower.

- `false` no initial-state QED radiation,
- `true` initial-initial dipoles included (default).

This setting is included to facilitate comparisons with other tools and for efficiency improvements for quark initial states.

`PDF_MIN_X` This setting controls a threshold on the PDF or structure function ratio in the shower for numerical stability. The default is 10^{-2} , but the QED initial-state shower for leptons requires it to be set to 10^{-1} to resolve softer radiation.

To run SHERPA at NLO in the EW theory, the `NLO_Order` parameter in the `Process` section of the runcard must be set appropriately and the loop provider specified. In addition, the subtraction must be set as follows:

`NLO_SUBTRACTION_MODE` This setting controls which IR divergences are subtracted.

- `QCD` only QCD subtraction (default),
- `QED` only QED subtraction,
- `QCD+QED` all SM IR divergences will be subtracted.

The `MC@NLO` is turned on in the usual way, using `NLO_MODE: MC@NLO` and the associated settings. Some settings are read from the `SHOWER` equivalents but some are set separately for `MC@NLO`, please check the latest manual for details.

References

- [1] M. Benedikt et al., FCC, *Future Circular Collider Feasibility Study Report: Volume 1, Physics, Experiments, Detectors*, [arXiv:2505.00272](#) [hep-ex].
- [2] P. Nason, *A New method for combining NLO QCD with shower Monte Carlo algorithms*, JHEP **11** (2004), 040, [[hep-ph/0409146](#)].
- [3] S. Frixione and B. R. Webber, *Matching NLO QCD computations and parton shower simulations*, JHEP **06** (2002), 029, [[hep-ph/0204244](#)].
- [4] S. Jadach, W. Płaczek, S. Sapeta, A. Siódmok and M. Skrzypek, *Matching NLO QCD with parton shower in Monte Carlo scheme — the KrkNLO method*, JHEP **10** (2015), 052, [[arXiv:1503.06849](#) [hep-ph]].
- [5] L. Lönnblad and S. Prestel, *Merging Multi-leg NLO Matrix Elements with Parton Showers*, JHEP **03** (2013), 166, [[arXiv:1211.7278](#) [hep-ph]].
- [6] P. Nason and G. P. Salam, *Multiplicative-accumulative matching of NLO calculations with parton showers*, JHEP **01** (2022), 067, [[arXiv:2111.03553](#) [hep-ph]].
- [7] M. van Beekveld, S. Ferrario Ravasio, J. Helliwell, A. Karlberg, G. P. Salam, L. Scyboz, A. Soto-Ontoso, G. Soyez and S. Zanolini, *Logarithmically-accurate and positive-definite NLO shower matching*, JHEP **10** (2025), 038, [[arXiv:2504.05377](#) [hep-ph]].
- [8] S. Catani, F. Krauss, R. Kuhn and B. R. Webber, *QCD matrix elements + parton showers*, JHEP **11** (2001), 063, [[hep-ph/0109231](#)].
- [9] L. Lönnblad, *Correcting the color dipole cascade model with fixed order matrix elements*, JHEP **05** (2002), 046, [[hep-ph/0112284](#)].
- [10] F. Krauss, *Matrix elements and parton showers in hadronic interactions*, JHEP **08** (2002), 015, [[hep-ph/0205283](#)].
- [11] J. Alwall et al., *Comparative study of various algorithms for the merging of parton showers and matrix elements in hadronic collisions*, Eur. Phys. J. C **53** (2008), 473–500, [[arXiv:0706.2569](#) [hep-ph]].
- [12] S. Höche, F. Krauss, S. Schumann and F. Siegert, *QCD matrix elements and truncated showers*, JHEP **05** (2009), 053, [[arXiv:0903.1219](#) [hep-ph]].
- [13] S. Höche, F. Krauss, M. Schönherr and F. Siegert, *QCD matrix elements + parton showers: The NLO case*, JHEP **04** (2013), 027, [[arXiv:1207.5030](#) [hep-ph]].
- [14] T. Gehrmann, S. Hoche, F. Krauss, M. Schonherr and F. Siegert, *NLO QCD matrix elements + parton showers in $e^+e^- \rightarrow$ hadrons*, JHEP **01** (2013), 144, [[arXiv:1207.5031](#) [hep-ph]].
- [15] R. Frederix and S. Frixione, *Merging meets matching in MC@NLO*, JHEP **12** (2012), 061, [[arXiv:1209.6215](#) [hep-ph]].
- [16] S. Plätzer, *Controlling inclusive cross sections in parton shower + matrix element merging*, JHEP **08** (2013), 114, [[arXiv:1211.5467](#) [hep-ph]].
- [17] G. Ferrera, G. Somogyi and F. Tramontano, *Associated production of a Higgs boson decaying into bottom quarks at the LHC in full NNLO QCD*, Phys. Lett. B **780** (2018), 346–351, [[arXiv:1705.10304](#) [hep-ph]].
- [18] S. Caletti, A. Gehrmann-De Ridder and M. Marcoli, *NNLO QCD predictions for jet observables in ZH production at electron-positron colliders*, [arXiv:2510.20485](#) [hep-ph].
- [19] E. A. Kuraev and V. S. Fadin, *On Radiative Corrections to e^+e^- Single Photon Annihilation at High-Energy*, Sov. J. Nucl. Phys. **41** (1985), 466–472.
- [20] D. R. Yennie, S. C. Frautschi and H. Suura, *The infrared divergence phenomena and high-energy processes*, Annals Phys. **13** (1961), 379–452.

- [21] S. Jadach, B. F. L. Ward and Z. Was, *The Precision Monte Carlo event generator K K for two fermion final states in e^+e^- collisions*, Comput. Phys. Commun. **130** (2000), 260–325, [[hep-ph/9912214](#)].
- [22] F. Krauss, A. Price and M. Schönherr, *YFS Resummation for Future Lepton-Lepton Colliders in SHERPA*, SciPost Phys. **13** (2022), no. 2, 026, [[arXiv:2203.10948](#) [hep-ph]].
- [23] T. Sjostrand, *A Model for Initial State Parton Showers*, Phys. Lett. B **157** (1985), 321–325, FERMILAB-PUB-85-023-T.
- [24] G. Balossini, C. M. Carloni Calame, G. Montagna, O. Nicrosini and F. Piccinini, *Matching perturbative and parton shower corrections to Bhabha process at flavour factories*, Nucl. Phys. B **758** (2006), 227–253, [[hep-ph/0607181](#)].
- [25] E. Budassi, C. M. Carloni Calame, M. Ghilardi, A. Gurgone, G. Montagna, M. Moretti, O. Nicrosini, F. Piccinini and F. P. Ucci, *Radiative return at NLOPS accuracy*, [arXiv:2601.19530](#) [hep-ph].
- [26] L. P. Flower, *Automated inclusion of QED corrections in Monte Carlo event generators*, Ph.D. thesis, Durham U., Durham U., IPPP, 2024.
- [27] R. Aliberti et al., *Radiative corrections and Monte Carlo tools for low-energy hadronic cross sections in e^+e^- collisions*, SciPost Phys. **9** (2024), , [[arXiv:2410.22882](#) [hep-ph]].
- [28] S. Catani and M. H. Seymour, *A General algorithm for calculating jet cross-sections in NLO QCD*, Nucl. Phys. **B485** (1997), 291–419, [[arXiv:hep-ph/9605323](#) [hep-ph]], [Erratum: Nucl. Phys.B510,503(1998)].
- [29] S. Catani, S. Dittmaier, M. H. Seymour and Z. Trocsanyi, *The Dipole formalism for next-to-leading order QCD calculations with massive partons*, Nucl. Phys. **B627** (2002), 189–265, [[arXiv:hep-ph/0201036](#) [hep-ph]].
- [30] M. Schönherr, *An automated subtraction of NLO EW infrared divergences*, Eur. Phys. J. **C78** (2018), no. 2, 119, [[arXiv:1712.07975](#) [hep-ph]].
- [31] S. Kallweit, J. M. Lindert, S. Pozzorini and M. Schönherr, *NLO QCD+EW predictions for $2\ell 2\nu$ diboson signatures at the LHC*, JHEP **11** (2017), 120, [[arXiv:1705.00598](#) [hep-ph]].
- [32] S. Schumann and F. Krauss, *A Parton shower algorithm based on Catani-Seymour dipole factorisation*, JHEP **03** (2008), 038, [[arXiv:0709.1027](#) [hep-ph]].
- [33] S. Höche, S. Schumann and F. Siegert, *Hard photon production and matrix-element parton-shower merging*, Phys. Rev. D **81** (2010), 034026, [[arXiv:0912.3501](#) [hep-ph]].
- [34] M. Bengtsson and T. Sjostrand, *A Comparative Study of Coherent and Noncoherent Parton Shower Evolution*, Nucl. Phys. B **289** (1987), 810–846, LU-TP-86-24.
- [35] M. H. Seymour, *Matrix element corrections to parton shower algorithms*, Comput. Phys. Commun. **90** (1995), 95–101, [[hep-ph/9410414](#)].
- [36] T. Sjostrand, S. Mrenna and P. Z. Skands, *PYTHIA 6.4 Physics and Manual*, JHEP **05** (2006), 026, [[hep-ph/0603175](#)].
- [37] S. Höche, F. Krauss, M. Schönherr and F. Siegert, *A critical appraisal of NLO+PS matching methods*, JHEP **09** (2012), 049, [[arXiv:1111.1220](#) [hep-ph]].
- [38] Plätzer, Simon and Sjö Dahl, Malin, *The Sudakov Veto Algorithm Reloaded*, Eur. Phys. J. Plus **127** (2012), 26, [[arXiv:1108.6180](#) [hep-ph]].
- [39] L. Lönnblad, *Fooling Around with the Sudakov Veto Algorithm*, Eur. Phys. J. C **73** (2013), no. 3, 2350, [[arXiv:1211.7204](#) [hep-ph]].
- [40] T. Carli, T. Gehrmann and S. Höche, *Hadronic final states in deep-inelastic scattering with Sherpa*, Eur. Phys. J. C **67** (2010), 73–97, [[arXiv:0912.3715](#) [hep-ph]].
- [41] S. Höche, F. Krauss and M. Schönherr, *Uncertainties in MEPS@NLO calculations of h +jets*, Phys. Rev. D **90** (2014), no. 1, 014012, [[arXiv:1401.7971](#) [hep-ph]].

- [42] G. Aad et al., ATLAS, *Modelling and computational improvements to the simulation of single vector-boson plus jet processes for the ATLAS experiment*, JHEP **08** (2022), 089, [arXiv:2112.09588 [hep-ex]].
- [43] S. J. Brodsky, G. P. Lepage and P. B. Mackenzie, *On the Elimination of Scale Ambiguities in Perturbative Quantum Chromodynamics*, Phys. Rev. D **28** (1983), 228, SLAC-PUB-3011, FERMILAB-PUB-83-040-T.
- [44] A. Buckley et al., *General-purpose event generators for LHC physics*, Phys. Rept. **504** (2011), 145–233, [arXiv:1101.2599 [hep-ph]].
- [45] C. Bierlich et al., *A comprehensive guide to the physics and usage of PYTHIA 8.3*, arXiv:2203.11601 [hep-ph].
- [46] G. S. Chahal and F. Krauss, *Cluster Hadronisation in Sherpa*, SciPost Phys. **13** (2022), no. 2, 019, [arXiv:2203.11385 [hep-ph]].
- [47] S. Dittmaier, *A general approach to photon radiation off fermions*, Nucl. Phys. **B565** (2000), 69–122, [arXiv:hep-ph/9904440 [hep-ph]].
- [48] S. Dittmaier, A. Kabelschacht and T. Kasprzik, *Polarized QED splittings of massive fermions and dipole subtraction for non-collinear-safe observables*, Nucl. Phys. **B800** (2008), 146–189, [arXiv:0802.1405 [hep-ph]].
- [49] S. Frixione, *Initial conditions for electron and photon structure and fragmentation functions*, JHEP **11** (2019), 158, [arXiv:1909.03886 [hep-ph]].
- [50] M. Stahlhofen, *NNLO electron structure functions (PDFs) from SCET*, JHEP **11** (2025), 171, [arXiv:2508.16964 [hep-ph]].
- [51] M. Schnubel and R. Szafron, *Electron and Photon Structure Functions at Two Loops*, arXiv:2509.09618 [hep-ph].
- [52] S. Jadach, *private communication*.
- [53] S. Höche and M. Schönherr, *Uncertainties in next-to-leading order plus parton shower matched simulations of inclusive jet and dijet production*, Phys. Rev. D **86** (2012), 094042, [arXiv:1208.2815 [hep-ph]].
- [54] G. Balossini, C. Bignamini, C. M. C. Calame, G. Montagna, O. Nicrosini and F. Piccinini, *Photon pair production at flavour factories with per mille accuracy*, Phys. Lett. B **663** (2008), 209–213, [arXiv:0801.3360 [hep-ph]].
- [55] E. Budassi, C. M. Carloni Calame, M. Ghilardi, A. Gurgone, G. Montagna, M. Moretti, O. Nicrosini, F. Piccinini and F. P. Ucci, *Pion pair production in e^+e^- annihilation at next-to-leading order matched to Parton Shower*, JHEP **05** (2025), 196, [arXiv:2409.03469 [hep-ph]].
- [56] Z. Nagy, *Next-to-leading order calculation of three jet observables in hadron hadron collision*, Phys. Rev. **D68** (2003), 094002, [arXiv:hep-ph/0307268 [hep-ph]].
- [57] S. Höche, F. Krauss, M. Schönherr and F. Siegert, *NLO matrix elements and truncated showers*, JHEP **08** (2011), 123, [arXiv:1009.1127 [hep-ph]].
- [58] A. Denner and S. Dittmaier, *Electroweak Radiative Corrections for Collider Physics*, Phys. Rept. **864** (2020), 1–163, [arXiv:1912.06823 [hep-ph]].
- [59] N. Greiner and M. Schönherr, *NLO QCD+EW corrections to diphoton production in association with a vector boson*, JHEP **01** (2018), 079, [arXiv:1710.11514 [hep-ph]].
- [60] C. Gütschow and M. Schönherr, *Four lepton production and the accuracy of QED FSR*, Eur. Phys. J. C **81** (2021), no. 1, 48, [arXiv:2007.15360 [hep-ph]].
- [61] D. Pagani, H.-S. Shao, I. Tsinikos and M. Zaro, *Automated EW corrections with isolated photons: $t\bar{t}\gamma$, $t\bar{t}\gamma\gamma$ and $t\bar{t}j$ as case studies*, JHEP **09** (2021), 155, [arXiv:2106.02059 [hep-ph]].

- [62] F. Krauss, R. Kuhn and G. Soff, *AMEGIC++ 1.0: A Matrix element generator in C++*, JHEP **02** (2002), 044, [[arXiv:hep-ph/0109036](#) [hep-ph]].
- [63] T. Gleisberg and S. Höche, *Comix, a new matrix element generator*, JHEP **12** (2008), 039, [[arXiv:0808.3674](#) [hep-ph]].
- [64] F. Buccioni, J.-N. Lang, J. M. Lindert, P. Maierhöfer, S. Pozzorini, H. Zhang and M. F. Zoller, *OpenLoops 2*, Eur. Phys. J. C **79** (2019), no. 10, 866, [[arXiv:1907.13071](#) [hep-ph]].
- [65] A. Denner, S. Dittmaier and L. Hofer, *Collier: a fortran-based Complex One-Loop Library in Extended Regularizations*, Comput. Phys. Commun. **212** (2017), 220–238, [[arXiv:1604.06792](#) [hep-ph]].
- [66] G. Ossola, C. G. Papadopoulos and R. Pittau, *CutTools: A Program implementing the OPP reduction method to compute one-loop amplitudes*, JHEP **03** (2008), 042, [[arXiv:0711.3596](#) [hep-ph]].
- [67] A. van Hameren, *OneLOop: For the evaluation of one-loop scalar functions*, Comput. Phys. Commun. **182** (2011), 2427–2438, [[arXiv:1007.4716](#) [hep-ph]].
- [68] A. Denner, S. Dittmaier, M. Roth and L. H. Wieders, *Electroweak corrections to charged-current $e^+e^- \rightarrow 4$ fermion processes: Technical details and further results*, Nucl. Phys. **B724** (2005), 247–294, [[arXiv:hep-ph/0505042](#) [hep-ph]], [Erratum: Nucl. Phys. **B854**, 504(2012)].
- [69] L. Flower and M. Schönherr, *Photon splitting corrections to soft-photon resummation*, JHEP **03** (2023), 238, [[arXiv:2210.07007](#) [hep-ph]].
- [70] F. Belloni, M. Chiesa, C. Oleari and E. Re, *Towards the inclusion of NLO EW corrections in the MiNLO method in Drell-Yan processes*, [arXiv:2602.16029](#) [hep-ph].
- [71] S. Höche, S. Kuttimalai, S. Schumann and F. Siegert, *Beyond Standard Model calculations with Sherpa*, Eur. Phys. J. C **75** (2015), no. 3, 135, [[arXiv:1412.6478](#) [hep-ph]].
- [72] M. Schönherr and F. Krauss, *Soft Photon Radiation in Particle Decays in SHERPA*, JHEP **12** (2008), 018, [[arXiv:0810.5071](#) [hep-ph]].
- [73] E. Bothmann et al., *Sherpa, Event generation with Sherpa 3*, JHEP **12** (2024), 156, [[arXiv:2410.22148](#) [hep-ph]].
- [74] L. Flower, J. Roper and M. Schönherr, *in preparation*.
- [75] V. Bertone, M. Cacciari, S. Frixione and G. Stagnitto, *The partonic structure of the electron at the next-to-leading logarithmic accuracy in QED*, JHEP **03** (2020), 135, [[arXiv:1911.12040](#) [hep-ph]], [Erratum: JHEP **08**, 108 (2022)].
- [76] S. Frixione, *On factorisation schemes for the electron parton distribution functions in QED*, JHEP **07** (2021), 180, [[arXiv:2105.06688](#) [hep-ph]], [Erratum: JHEP **12**, 196 (2012)].
- [77] A. Buckley et al., *Rivet user manual*, Comput. Phys. Commun. **184** (2013), 2803–2819, [[arXiv:1003.0694](#) [hep-ph]].
- [78] C. Bierlich et al., *Robust Independent Validation of Experiment and Theory: Rivet version 3*, SciPost Phys. **8** (2020), 026, [[arXiv:1912.05451](#) [hep-ph]].
- [79] C. Bierlich, A. Buckley, J. M. Butterworth, C. Gutsche, L. Lonnblad, T. Procter, P. Richardson and Y. Yeh, *Robust independent validation of experiment and theory: Rivet version 4 release note*, SciPost Phys. Codeb. **36** (2024), 1, [[arXiv:2404.15984](#) [hep-ph]].
- [80] S. Frixione, *On factorisation schemes for the electron parton distribution functions in QED*, JHEP **07** (2021), 180, [[arXiv:2105.06688](#) [hep-ph]], [Erratum: JHEP **12**, 196 (2012)].
- [81] T. Gleisberg and F. Krauss, *Automating dipole subtraction for QCD NLO calculations*, Eur. Phys. J. **C53** (2008), 501–523, [[arXiv:0709.2881](#) [hep-ph]].
- [82] F. Krauss and D. Napoletano, *Towards a fully massive five-flavour scheme*, [arXiv:1712.06832](#) [hep-ph].

- [83] S. Forte, T. Giani and D. Napoletano, *Fitting the b -quark PDF as a massive- b scheme: Higgs production in bottom fusion*, Eur. Phys. J. C **79** (2019), no. 7, 609, [[arXiv:1905.02207](#) [hep-ph]].
- [84] F. Caola, K. Melnikov, D. Napoletano and L. Tancredi, *Noncancellation of infrared singularities in collisions of massive quarks*, Phys. Rev. D **103** (2021), no. 5, 054013, [[arXiv:2011.04701](#) [hep-ph]].
- [85] R. Gauld, *A massive variable flavour number scheme for the Drell-Yan process*, SciPost Phys. **12** (2022), no. 1, 024, [[arXiv:2107.01226](#) [hep-ph]].
- [86] J. Harz, M. Klasen, M. Y. Sassi and L. P. Wiggering, *Dipole formalism for massive initial-state particles and its application to dark matter calculations*, Phys. Rev. D **107** (2023), no. 5, 056020, [[arXiv:2210.03409](#) [hep-ph]].
- [87] M. Guzzi, P. Nadolsky, L. Reina, D. Wackerroth and K. Xie, *General mass variable flavor number scheme for Z boson production in association with a heavy quark at hadron colliders*, Phys. Rev. D **110** (2024), no. 11, 114030, [[arXiv:2410.03876](#) [hep-ph]].